Lifetimes of confined optical phonons and the shape of a Raman peak in disordered nanoparticles. II. Numerical treatment

Sergei V. Koniakhin [1,2,*] Oleg I. Utesov,[3,4,†] and Andrey G. Yashenkin[3,4]

[1]*Institute Pascal, PHOTON-N2, University Clermont Auvergne, CNRS, 4 Avenue Blaise Pascal, Aubière Cedex 63178, France*

[2]*St. Petersburg Academic University - Nanotechnology Research and Education Centre of the Russian Academy of Sciences, St. Petersburg 194021, Russia*

[3]*Petersburg Nuclear Physics Institute NRC "Kurchatov Institute", Gatchina 188300, Russia*

[4]*Department of Physics, St. Petersburg State University, St. Petersburg 199034, Russia*

(Received 16 July 2020; accepted 22 October 2020; published 16 November 2020)

Disorder-induced broadening of optical vibrational eigenmodes in nanoparticles of nonpolar crystals is studied numerically. The methods previously used to treat the phonons in defectless particles are adjusted for numerical evaluation of the disordered problem. Imperfections in the forms of Gaussian and binary disorders as well as surface irregularities are investigated thoroughly in a wide range of impurity concentrations and disorder strengths. For dilute and weak pointlike impurities the regimes of separated and overlapped phonon levels are obtained and the behavior of the linewidth predicted analytically is confirmed; the crossover scale falls into the actual range of several nanometers. These notions survive for strong dilute impurities, as well. Regimes and crossovers predicted by the analytical approach are checked and identified, and the minor discrepancies are discussed. We mention a few of them: slower than in analytics increasing of the linewidth with the phonon quantum number for weak disorder and only a qualitative agreement between analytics and numerics for the resonant broadening in strong dilute disorder. The novel phenomena discovered numerically are the "mesoscopic smearing" of the distribution function in the ensemble of identical disordered particles, an inflection of the linewidth dependence on the impurity concentration for light "dense" binary impurities, and a position-dependent capability of a strong impurity to catch the phonon. It is shown that surface irregularities contribute to the phonon linewidth less than the volume disorder, and their rates reveal faster decay with increasing of the particle size. It is argued that the results of the present research are applicable also for quantum dots and short quantum wires.

DOI: 10.1103/PhysRevB.102.205422

I. INTRODUCTION

Manufacturing, characterization, investigation, and application of diverse small particles and, particularly, of crystalline dielectric and semiconducting nanoparticles are among the most important and intensively developing areas of contemporary scientific research and technology. The role of nanoparticle studies in domains of optics, quantum computing, chemistry, and materials science permanently grows [1–9]; various applications of nanoparticles penetrate biology and medicine, the nanoparticles being used as dyes, carriers, and imaging systems [10–15]. This imposes the strict necessity for tools and methods of their physical and chemical characterization [16,17]; the particle size is an important parameter to know. Such experimental techniques as atomic force microscopy, dynamic light scattering, transmission electron microscopy, calorimetry, x-ray diffraction, Raman spectroscopy, etc., have been used for these purposes [18–30].

The Raman spectroscopy is sensitive to the finite-size quantization of wave vectors of optical phonons taking place in particles. As a result, the Raman peak for a particle is redshifted comparing to the bulk material [31]. Since the introduction of the phonon confinement model (PCM) it has become possible to connect this shift with the particle size and therefore to adjust the Raman spectroscopy for size probing [32]. However, the PCM approach remains completely phenomenological. Moreover, for the smallest nanoparticles it produces very inaccurate results [33–37]. Numerous efforts undertaken to modify the PCM and to enhance the quality of analysis of the experiment [22,38–43] did not change this situation principally.

Recently, two mutually related novel descriptions [33,34] of Raman experiments in nanopowders of nonpolar crystals have been proposed to replace the PCM. Both of these descriptions utilize a microscopic approach and therefore both have more solid grounds. Unfortunately, these theories (as well as the PCM) incorporate the linewidth of the optical vibrational eigenmode as a fitting parameter.

The theory developed in Ref. [44] and in the present paper (hereinafter papers I and II, respectively) is the microscopic approach to the disorder-induced phonon line broadening of optical modes in nanoparticles which accomplishes the theory of Raman spectra of nanopowders of nonpolar crystals of Refs. [33,34]. This method is much more precise and well grounded than the PCM. In particular, it allows us to extract

*kon@mail.ioffe.ru
†utiosov@gmail.com

from the Raman data four parameters of a nanopowder, such as the mean size of the particles L, the standard deviation of the size distribution function δL, the particle shape parametrized by the effective faceting number p (elongated particles are not considered), and the strength of intrinsic disorder S [44] (see also [45]).

Paper I is devoted to the analytical treatment of this problem. Both spectral weights and linewidths Γ_n of eigenmodes are calculated as the functions of their quantum number n, nanoparticle shape, its size, and the strength of disorder within the framework of three models, namely for Born impurities, in the smooth random impurity potential, and for strong binary disorder. The results are drastically different for the cases of separated phonon levels and for levels belonging to the continuum.

This paper is a numerical continuation of paper I; however, its outcome is not only the numerical verification of formulas obtained in Ref. [44] but also the report of several essentially new results such as the "mesoscopic smearing" of the size distribution function or the dependence of the capability for strong impurity to localize the phonon mode on its location in the particle. Even more importantly, our numerical approach allows us to deal with more physical realizations of disorder such as the so-called NV (nitrogen + vacancy) centers in diamonds. Furthermore, sophisticated and hardly analytically expressible types of disorder (e.g., the surface corrugations) are also investigated.

We adopt the more general DMM-BPM method [33] (dynamical matrix method–bond polarization model) and the EKFG method [34] (a continuous approach using the Euclidean Klein-Fock-Gordon equation) applied previously to study phonons in the pure particles for the numerical treatment of the disordered problem incorporating the procedure of averaging over disorder configurations into the formalism of Green's functions. We examine numerically (pointlike and smooth) Gaussian and (pointlike) binary disorders varying the impurity concentration c_{imp} and the local atomic mass defects $\delta m/m$ in the wide intervals but mostly focusing on the dilute regime $c_{\mathrm{imp}} \lesssim 0.1$. For the surface corrugations we introduce two models of disorder which we call the "peeled apples model" and the "nibbled apples model," which allows to investigate the (possible) scaling properties of the disorder.

The analytical predictions made for the weak pointlike impurities about the phonon linewidth dependencies in the form $\Gamma_n \propto \sqrt{S}/L^{3/2}$ for separated phonon levels and $\Gamma_n \propto S/L$ for the overlapped ones are confirmed numerically, and the spatial scale of the crossover between these regimes is estimated as lying within the nanometer range. We find that the phonon linewidth indeed grows with its quantum number but slower than predicted by the analytics. Investigating the smooth random potential we observe numerically a significant diminishing of $\Gamma(\sigma)$ that occurs at the characteristic disorder scale $\sigma \simeq L/2\pi$. We discover numerically and explain the phenomenon of broadening of the distribution function in an ensemble of identical disordered particles which we call the "mesoscopic smearing."

Next, examining numerically the phonons subject to a strong dilute disorder we find that the notions of separated and overlapped regimes with their specific c_{imp} and L dependencies for the phonon linewidth survive in this case, as well. For dense and very light binary impurities we detected a crossover to the novel regime $\Gamma_n \propto c_{\mathrm{imp}}^{3/2}/\sqrt{L}$ which originates from the multi-impurity scattering processes and from the proximity to the percolation transition. Inspecting the resonant impurity scattering and the formation of the optical phonon-impurity (localized) bound state we report a good qualitative agreement between the results of numerical experiment and the analytics. The new phenomenon seen in the numerics is a rapid decay with the distance from the center of a particle observed for the ability of a strong impurity to capture the phonon mode.

At first, the role of surface corrugations of a particle in the broadening of the volume optical phonon modes investigated numerically in the present paper is shown to be essentially smaller as compared to the volume imperfections. Typically, the surface disorder could not even lead to an overlap of the main optical mode. For separated levels we find $\Gamma_1 \propto \sqrt{c_{\mathrm{imp}}}/L^2$ and $\Gamma_1 \propto \sqrt{c_{\mathrm{imp}}}/L^4$ dependencies for this mode provided that the disorder scales with the particle size and does not scale, respectively. The phonon line broadening due to surface disorder strongly increases with its quantum number, though.

We observe visually an asymmetry of the phonon lines and their non-Lorentzian shapes predicted in paper I.

The paper is organized as follows. In Sec. II we formulate the methods we used to study the pure problem and adopt them for numerical treatment of disordered particles. Section III sketches the sources and the peculiarities of disorder in nanopowders and specifies their relations to the models considered. Section IV is devoted to the analysis of weak disorder (including its pointlike and smooth versions); it also addresses the phenomenon of "mesoscopic smearing." In Sec. V we investigate the strong dilute impurities (including their resonant and unitary regimes) and the crossover to the "dense" regime of concentrations. In Sec. VI we examine the role of surface corrugations. The last section, Sec. VII, contains the summary of our results and their discussion.

II. METHODS

In Secs. II A and II B we briefly sketch the methods (DMM-BPM and EKFG) we shall use in order to characterize the Raman scattering. Section II C is devoted to the description of the Green's function formalism adapted for disordered particles.

A. Dynamical matrix method: Atomistic approach

The dynamical matrix method (DMM) [46,47] provides a very good accuracy of derivation of normal vibrational eigenmodes and the corresponding eigenfrequencies for multicomponent quantum objects such as molecules and nanoparticles. It consists of solving the $3N \times 3N$ matrix eigenvalue problem formulated for the system of Newton's laws of motion for N atoms:

$$\omega^2 r_{l,\alpha} = \frac{1}{m_l} \sum_{l'=1}^{N} \sum_{\beta=x,y,z} \frac{\partial^2 \Phi}{\partial r_{l,\alpha} \partial r_{l',\beta}} r_{l',\beta}, \tag{1}$$

where $r_{l,\alpha}$ is the displacement of the lth atom along the direction α, m_l is the mass of the lth atom, and Φ is the total energy of the particle written as a function of atomic displacements.

The masses of atoms could be eliminated from Eqs. (1) by the local rescaling of variables $\xi_l = r_l\sqrt{m_l}$ for varying atomic masses and by the global rescaling $\xi_l = r_l\sqrt{m}$ for the identical ones. For translationally invariant crystals DMM yields the phonon dispersion and its polarization. The solution of the DMM problem determines displacements $r_{l,\alpha}(n)$ for each eigenmode n.

Since we choose nanodiamonds as a testing object for our approach we construct the dynamical matrix utilizing the elastic parameters of the diamond lattice extracted from the microscopic Keating model [48–51]. Within this model parameter α_0 measures the bond rigidity with respect to stretching and parameter β_0 is responsible for the valence angle bending. We use the values $\alpha_0 = 1.068$ dyn cm^{-2} and $\beta_0 = 0.821$ dyn cm^{-2} from Table II of Ref. [52].

For the dispersion of optical phonons we utilize the conventional expression

$$\omega_{\mathbf{q}} = A + B\cos(qa_0/2), \tag{2}$$

where $a_0 = 0.357$ nm is the diamond lattice constant. The Keating model and the employed force constants yield $A + B = \omega_0 \approx 1333$ cm^{-1} and $B \approx 85$ cm^{-1}. Near the Brillouin zone center the dispersion simplifies [44]:

$$\omega_{\mathbf{q}} = \omega_0[1 - F(qa_0)^2], \tag{3}$$

and F measures the spectrum flatness. Comparing Eq. (3) with the Taylor expansion of Eq. (2), we get $F = \frac{B}{8(A+B)}$.

B. Euclidean Klein-Fock-Gordon equation: Continuous media approach

Another approach to the Raman spectra of nanoparticles is developed in Ref. [34]. It utilizes a continuous description of the long-wavelength optical phonons and the continuous version of the BPM. Within the framework of the EKFG method the phonon wave functions Y satisfy the following differential equation with the Dirichlet boundary conditions ($\partial\Omega$ being the particle boundary):

$$\left(\partial_t^2 + C_1\Delta + C_2\right)Y = 0, \quad Y|_{\partial\Omega} = 0. \tag{4}$$

The eigenfrequencies can be obtained as

$$\omega^2 = C_2 - C_1 q^2, \tag{5}$$

where q^2 is the eigennumber of the problem

$$\Delta Y + q^2 Y = 0, \quad Y|_{\partial\Omega} = 0. \tag{6}$$

Within the range of validity of the EKFG approach (small $q \ll a_0^{-1}$) the phonon frequency of a mode with the generalized quantum number n reads

$$\omega_n \approx \sqrt{C_2} - \frac{C_1}{\sqrt{C_2}}\frac{q_n^2}{2}. \tag{7}$$

Since Eq. (7) should be a quantized version of Eq. (3) one obtains $C_2 = (A + B)^2$ and $C_1 = a_0^2 B(A + B)/4$.

The main advantage of the EKFG approach is its relative simplicity. Equation (6) can be solved analytically for cubic, spherical, and cylindrical particles and numerically for other particle shapes using standard methods which are included, e.g., in the Mathematica package [53].

Importantly, both of the above-mentioned approaches can be easily adopted for the numerical treatment. Moreover, the EKFG approach allows us to manipulate with larger particles inaccessible by means of DMM. In our further analysis, we will combine both of these methods.

C. Phonon propagator in disordered particles

Here we adopt the formalism of the phonon Green's functions for the treatment of disordered particles. Let n enumerate the eigenstates of a pure particle while the variable ε spans the energies of eigenstates in the ensemble of disordered particles; the eigenfunctions of these states are $|n\rangle$ and $|\varepsilon\rangle$, respectively. The propagator of the nth phonon mode has the form [54]

$$\begin{aligned} D_n(t) &= i\langle \mathrm{vac}|\hat{\mathrm{T}}(b_n^\dagger(t) - b_n(t))[b_n^\dagger(0) - b_n(0)]|\mathrm{vac}\rangle \\ &= -i\,\theta(t)\langle n|e^{-i\mathcal{H}t}|n\rangle - i\,\theta(-t)\langle n|e^{i\mathcal{H}t}|n\rangle \\ &= -i\sum_\varepsilon |\langle n|\varepsilon\rangle|^2[\theta(t)e^{-i\varepsilon t} + \theta(-t)e^{i\varepsilon t}]. \end{aligned} \tag{8}$$

Here $\hat{\mathrm{T}}$ is the time-ordering operator, $b_n^\dagger$ (b_n) are the creation (annihilation) operators acting on pure eigenstates, $\theta(t)$ is the Heaviside theta function, and $\mathcal{H}$ is the Hamiltonian of the disordered problem. After the Fourier transform we obtain the propagator

$$D_n(\omega) = \sum_\varepsilon |\langle n|\varepsilon\rangle|^2\left(\frac{1}{\omega - \varepsilon + i0} - \frac{1}{\omega + \varepsilon - i0}\right). \tag{9}$$

Near the positive pole its imaginary part reads

$$\mathrm{Im}\, D_n(\omega) = -\pi\sum_\varepsilon \delta(\omega - \varepsilon)|\langle n|\varepsilon\rangle|^2. \tag{10}$$

Averaging Eq. (10) over disorder configurations (which is denoted by the overline) we calculate the density of states $\rho(\omega)$:

$$\overline{\mathrm{Im}\, D_n(\omega)} = -\pi\,\rho(\omega)\overline{|\langle n|\omega\rangle|^2}. \tag{11}$$

This quantity multiplied by $-\pi^{-1}$ represents the spectral weight of a broadened vibrational eigenmode. Using the Lorentz approximation for the spectral weight we obtain the linewidth for the nth mode.

In order to perform the disorder averaging in Eq. (10) one should specify the type of disorder. Within the DMM approach we deal with the eigenfunctions $r(k, n)_{l,\alpha}$, where k stands for the index of disorder realization (we reserve the value $k = 0$ for the pure particle). Then Eq. (11) becomes

$$\begin{aligned} \overline{\mathrm{Im}\, D_n(\omega)} = -\frac{\pi}{N_c}\sum_{k=1}^{N_c}\sum_{n'=1}^{3N}\delta(\omega - \omega_{n'}) \\ \times\left[\sum_{l=1}^{N}\sum_{\alpha=x,y,z} r(0, n)_{l,\alpha}\, r(k, n')_{l,\alpha}\right]^2, \end{aligned} \tag{12}$$

where N_c is the number of configurations. In order to distinguish visually between DMM-BPM and EKFG formulas we denote the eigenfunctions as $r(k, n)_{l,\alpha}$ in the former case and as $Y_n(k, \mathbf{r})$ in the latter one which differs from the notations of Ref. [44]. In real calculations we replaced the upper limit in the inner sum (the number of eigenmodes $3N$) by the energy cutoff $\omega_c = 1000$ cm^{-1} in order to prevent the mixing of

optical and acoustic modes at large momenta. This is justified by the fact that we never observed the broadening reaching the value $\sim 10^2$ cm^{-1} even for unrealistically strong disorder.

For continuous EKFG calculations the analog of Eq. (12) reads

$$\overline{\mathrm{Im}\, D_n(\omega)} = -\frac{\pi}{N_c}\sum_{k=1}^{N_c}\sum_{n'=1}^{N'}\delta(\omega-\omega_{n'}) \times\left[\int_\Omega d^3\mathbf{r}\, Y_n(0,\mathbf{r})Y_{n'}(k,\mathbf{r})\right]^2, \qquad (13)$$

where Ω is the volume of a particle. The upper limit N' of the inner sum in Eq. (13) is chosen from the condition for the characteristic "wave vector" $k_c = \frac{\max Y'}{\max Y}$ to be smaller than the size of the Brillouin zone π/a_0, where the prime stands for the spatial derivative.

III. DISORDER

In Sec. III A we present a qualitative picture of various types of disorder existing in nanoparticles. The peculiarities of their numerical investigation within the framework of approaches outlined in Sec. II are discussed in Secs. III B, III C, III D, and III E.

A. Preliminary remarks

When addressing the phenomena responsible for disorder-induced broadening of the Raman peak in nanoparticles one should mention four principal mechanisms. The first one is due to "ordinary impurities." The substitutional impurities in diamonds are realized as the distortions of the dynamical matrix stemming from random replacements of carbon atoms by another isotope of the carbon (weak pointlike impurities) or by another sort of atom (e.g., by nitrogen which forms the so-called NV centers [55] identified below as the strong pointlike impurities). These local variations of masses and rigidities scatter the vibrational modes and therefore provide their damping [see Fig. 1(a)]. Although physically the masses and the rigidities vary simultaneously, in Ref. [44] for the sake of simplicity only the masses have been taken to be random.

The second mechanism is related to large-scale inclusions (gaseous or solid) often existing in nanoparticles, to lattice distortions (dislocation, etc.), and to slow changes of characteristics of the crystal caused by the evolution of external parameters (pressure, temperature, chemical composition of the atmosphere, etc.) during the time of crystal growth. All these influences have a large-scale structure and could be regarded as "colored noise" with certain spatial scale σ exceeding the interatomic distance a_0 and comparable with the particle size L [see Fig. 1(b)]. We describe this type of disorder qualitatively by means of a smooth random (Gaussian) potential.

The third way to incorporate the disorder into the problem which is often referred to as the "surface corrugations" is specific for finite particles. It arises if one introduces the irregularities of the particle surface; the phonon scattering within the particle is due to the surface reflections whereas the interior of a crystal may be perfect for wave propagation [see Fig. 1(c)]. The surface scattering broadens the phonon line; the details of the broadening depend on the character of surface roughnesses. The correspondence between the propagation of electromagnetic (or electron) waves in irregular cavities and in regular cavities with spatial disorder was widely discussed in the late 1990s in terms of chaotization of dynamics in (both quantum and classical) "billiards" [56].

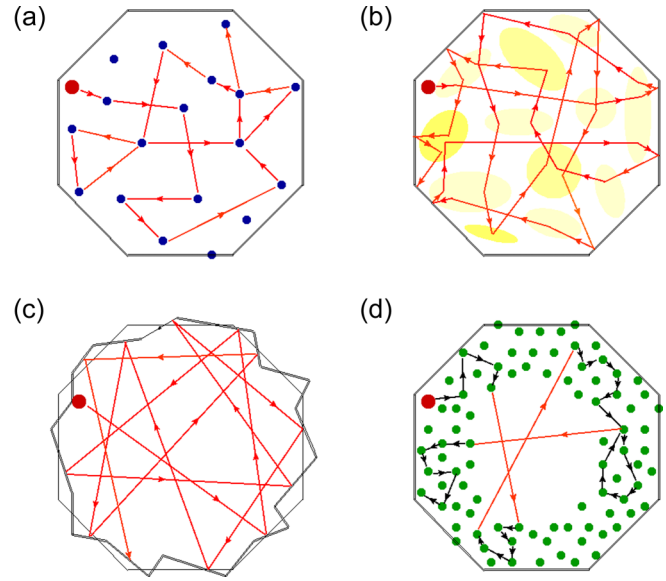

FIG. 1. The sketch of four types of disorder contributing to the phonon damping in nanoparticles. (a) The pointlike impurities located in the interior of a particle. Phonons propagate through the particle and sometimes scatter off the impurity. If the scattering occurs frequently (as in this picture), the phonon levels overlap. (b) A smooth disorder in the volume of a particle. The characteristic disorder scale σ is shorter than the particle size L. (c) The surface corrugations which can be considered as a random faceting of the particle. They lead to chaotization of propagating waves. (d) The shell of an amorphous phase near the surface of a particle. Vibrations propagating within this shell are not the phonons.

The fourth mechanism which leads to the Raman peak broadening in nanoparticles originates from surface amorphization [see Fig. 1(d)] well-documented for nanodiamonds [25,29,57,58]. It takes place within the near-surface shell of a crystal due to the crystal interference with a surrounding media during its growth and/or aging. The amorphous surface shell is also known to exist in bulk crystals, but its importance increases with increasing of the surface-to-bulk ratio, i.e., in nanoparticles. This mechanism implies a very strong disorder in the near-surface shell where even the notion of propagating wave (phonon) modes loses its meaning due to the lack of translational invariance. It is the only mechanism we shall not address in this paper. We postpone this issue to the forthcoming publications because it requires a principally different (critical-dynamics-like) analytical approach for its treatment and interpretation.

We believe that in real nanoparticles there is realized a certain combination of all four aforementioned mechanisms.

B. Binary disorder in discrete model

It is important to define a clear and meaningful measure of the disorder strength. Consider first the simplest binary

disorder, when the lattice sites are occupied with the probability $1 - c_{\rm imp}$ by the atoms with masses m and with the probability $c_{\rm imp}$ by the randomly placed impurities with masses $m + \delta m$. Here $c_{\rm imp} = N_i/N$ is the dimensionless concentration, N_i is the total number of impurities, and N is the total number of lattice sites in a particle. Then at low impurity concentrations $c_{\rm imp} \ll 1$ and for the small mass difference $\delta m/m \ll 1$ the disorder strength parameter could be introduced as follows:

$$S = c_{\rm imp}\left(\frac{\delta m}{m}\right)^2. \tag{14}$$

The mean variation of the binary disorder is not equal to zero, $\langle \delta m_i \rangle \neq 0$. The strength of the strong impurities with $|\delta m| \gtrsim m$ should be measured by the parameter

$$U = \frac{\delta m}{m + \delta m}, \tag{15}$$

still, under the condition $c_{\rm imp} \ll 1$. If $|U| \sim 1$ *and* $c_{\rm imp} \sim 1$, then the notion of the translational invariance (in any sense) disappears, and the solid becomes amorphous.

For diamonds, the binary distribution appears in two variants: as the isotopic disorder and in the form of substitutional nitrogen impurities. In the former case m corresponds to the ^{12}C atom and $m + \delta m$ is the ^{13}C atomic mass which yields $\delta m/m = (13 - 12)/12 = 1/12$. When the nitrogen atoms are considered, the effect is not so obvious. Normally, the nitrogen located in a diamond is accompanied by a vacancy in the lattice (NV center). These NV centers are in fact molecule-like complexes embedded into the carbon atoms surrounding which have the rich characteristic vibrational spectra [55,59]. The nitrogen atom possesses 5 electrons in the outer shell which are a subject of sp^3 hybridization: 3 of them form covalent bonds with the neighboring carbon atoms and 2 electrons related to the vacancy constitute a pair accompanied by an outer electron to form the NV^- center. The spectra of NV centers are quite intricate; in order to describe their fine structure one should engage the *ab initio* methods [60–62]. However, as far as the long-wavelength optical phonons are considered, all these peculiarities do not play significant role, and the phonons feel the NV defects as pointlike disturbances in the dynamical matrix of a diamond nanoparticle. Within the DMM approach we model the NV center as a vacancy neighboring the impurity with $\delta m/m = 0.17$; however, even simpler representation via a binary disorder with the unitary defects $U \to -\infty$ yields a pretty good result (see below).

C. Gaussian disorder in discrete model

For a Gaussian disorder, the masses of atoms are randomly distributed according to the Gaussian law around some mean value. Although precisely this form of disorder is rarely realized in practice, the model is very popular among the theorists for its analytical convenience. Moreover, the solution of the Gaussian problem reveals the majority of generic features shared by many physical types of disorder (see, e.g., Fig. 2). Therefore, the numerical study of the Gaussian disorder is the most straightforward way to verify the predictions of the analytical approach simultaneously staying on the physical grounds.

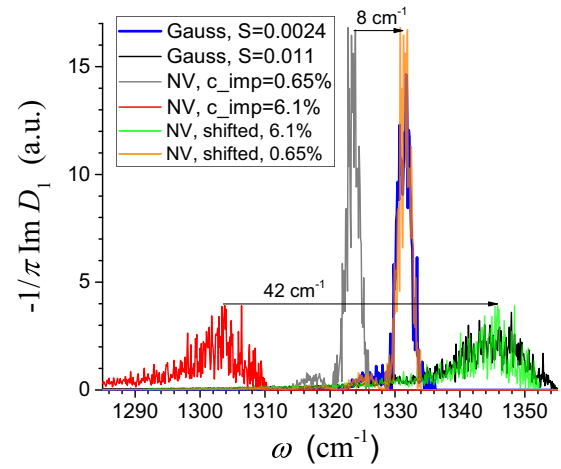

FIG. 2. The spectral weight of the first vibrational mode obtained using the DMM method and evaluated for the Gaussian disorder (blue and black curves) and for the binary disorder in the form of NV centers (gray and red curves) drawn for two values of the disorder corresponding to separated and overlapped regimes. The binary curves are significantly shifted with respect to the Gaussian ones due to nonzero value of $\langle \delta m_l \rangle$; however, after the substraction of these shifts (orange and green curves) the Gaussian and the binary line shapes became almost indistinguishable. Also, the line shapes calculated for the overlapped regime are asymmetric in agreement with the theory of paper I.

The definition (14) can be generalized onto an arbitrary distribution of the impurity masses:

$$S = \frac{\langle (\delta m_l)^2 \rangle}{m^2}, \tag{16}$$

where the nonzero contribution comes only from the impurity sites making the quantity S proportional to the impurity concentration $c_{\rm imp}$. The distribution function for a Gaussian disorder with $|\delta m|/m \ll 1$ is given by

$$\mathcal{F}(\delta m_l) = \frac{1}{\sqrt{2\pi S}} \exp\left[-\frac{(\delta m_l/m)^2}{2S}\right]. \tag{17}$$

For the purposes of the DMM-BPM method we model the weak Gaussian disorder as follows. The carbon-normalized inverse impurity mass $\tilde{m}^{-1}$ of the lth atom is chosen to be randomly varying within the interval $[0.25, 1.75]$ quantity with the probability

$$\mathcal{F}\left(\tilde{m}_l^{-1}\right) \propto \exp\left(-\frac{\left(\tilde{m}_l^{-1} - 1\right)^2}{2S}\right). \tag{18}$$

This procedure does not deliver zero for the average mass variation. Therefore, we add to each mass the value

$$\Delta\tilde{m}^{-1} = 1 - \frac{1}{N}\sum_{l=1}^{N} \tilde{m}_l^{-1}, \tag{19}$$

thus providing $\langle \delta m_l \rangle = 0$.

D. Disordered continuous EKFG model

Disorder can be incorporated into the continuous model by several means. The *pointlike* impurities of the discrete

DMM-BPM approach are mapped onto the spatial variation of the parameters $C_{1,2}$ in the EKFG equation. However, since the term with C_1 in Eq. (4) possesses an additional smallness due to the spatial derivatives we can vary only C_2:

$$\delta C_2(\mathbf{r}) = -\frac{\delta m(\mathbf{r})}{m + \delta m(\mathbf{r})} C_2. \tag{20}$$

Here m and C_2 stand for their values in the pure particle. Then for Born impurities one has

$$\langle \delta m(\mathbf{r}) \rangle = 0, \quad \frac{\langle \delta m(\mathbf{r}) \delta m(\mathbf{r}') \rangle}{m^2} = S V_0 \, \delta(\mathbf{r}' - \mathbf{r}), \tag{21}$$

where V_0 is the unit cell volume and S is the dimensionless strength of the impurities given by Eq. (16).

In our numerics we use the Mathematica package [53]. For Born impurities we reformulate the definition of the momentum q in Eq. (6) which can be rewritten in the form

$$\Delta Y + \frac{\delta C_2(\mathbf{r})}{C_1} Y + q^2 Y = 0, \quad Y|_{\partial\Omega} = 0. \tag{22}$$

Notice that the eigenfrequencies still can be found from Eq. (5), where C_2 corresponds to the pure particle. Then the procedure of generating new disorder configurations and numerically solving Eq. (22) should be performed repeatedly. The obtained eigenfunctions and eigenfrequencies are utilized in the subsequent calculation of the disorder-induced phonon line broadening (see Sec. II C).

In order to adopt the EKFG approach for the treatment of a *smooth* disorder let us introduce N_{def} defects providing the random Gaussian potential in the form

$$\delta C_2(\mathbf{r}) = \sum_{i=1}^{N_{\text{def}}} \frac{d_i C_2}{(2\pi\sigma^2)^{3/2}} e^{-\frac{(\mathbf{r}-\mathbf{r}_i)^2}{2\sigma^2}}, \tag{23}$$

where $\mathbf{r}_i$ are the centers of uncorrelated impurity potentials and d_i are the corresponding (Gaussian distributed) strength constants obeying the following conditions:

$$\langle d_i \rangle = 0, \quad \langle d_i d_j \rangle = \delta_{ij} S. \tag{24}$$

One can check that $\delta C_2(\mathbf{r}) \delta C_2(\mathbf{r}') \propto S$, and, performing disorder averaging $\langle \delta C_2(\mathbf{r}) \delta C_2(\mathbf{r}') \rangle$, the standard deviation is equal to σ; the latter result is valid if one neglects the boundary effects. Thus, we arrive to the problem investigated analytically in paper I.

When applying the continuous EKFG approach in order to investigate the more involved case of rare *strong* impurities we introduce N_{imp} unit cells in a particle ($N_{\text{imp}} \ll N$) with a fixed large value of $|\delta m|$ inside each of the cells.

E. Surface corrugations

We adjust the canonical EKFG approach for the analysis of an influence of particle surface irregularities on the phonon linewidth by solving the Laplace eigenproblem with the Dirichlet boundary conditions given by Eq. (6) for the shape of a boundary $\partial\Omega$ randomly varying from particle to particle under the constraint to preserve the particle volume. We examine in detail two particular models of the surface corrugations. The first one is the random triangular faceting of a cubic particle which yields the convex irregular polyhedron [hereinafter, the "peeled apples" model; see Fig. 3(a)]. For the second model we construct the particle using the cubic bricks of a certain size; some bricks on the surface are randomly removed with the probability c_{imp} [the "nibbled apples" model; see Fig. 3(b)]. These models differ by the type of surface irregularities whereas the volume of a particle is supposed to be clean in both cases.

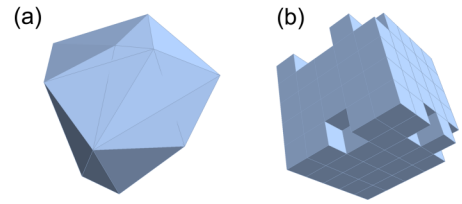

FIG. 3. (a) The particle with the random surface made of triangular facets ("peeled apples" model). This object is an example of the convex irregular polyhedron. (b) The particle made of cubic bricks with randomly removed bricks on the surface ("nibbled apples" model).

IV. RESULTS: WEAK IMPURITIES

In this section we present the results of numerical modeling for a weak (both pointlike and smooth) disorder and compare these results with the analytical predictions made in paper I. We also discuss the phenomenon of "mesoscopic smearing" not addressed in paper I. The disorder is assumed to be weak if not only the condition $S \ll 1$ is fulfilled but also its constituents c_{imp} and $(\delta m/m)^2$ are much smaller than unity *independently*.

A. Density of states and spectral weight

Let us discuss the behavior of the phonon density of states (DOS) in disordered nanodiamonds. The bulk DOS reveals the van Hove singularity at $\omega \to \omega_0$:

$$\rho(\omega \to \omega_0) = \frac{\theta(\omega_0 - \omega)\sqrt{\omega_0 - \omega}}{4\pi^2 (F\omega_0)^{3/2}}. \tag{25}$$

A more involved formula applicable in a wider frequency range can be found in Ref. [33]. The bulk DOS, together with the DOS functions calculated numerically for a 3 nm disordered spherical diamond (the number of atoms is ≈ 2450), is plotted in Fig. 4 as a function of frequency for different values of disorder; the disorder-induced shift of ω_0 is subtracted by hand. At the smallest S the phonon lines acquire just a little broadening much smaller than the energy spacings between different eigenmodes. The resulting DOS has a comblike structure similar to the DOS of a single particle. This DOS structure reproduces itself in the Raman spectrum, as it occurs, e.g., for fullerenes [63]. The observation of a comblike Raman spectrum for one nanoparticle or for an ensemble of very small, clean, and equal-sized nanoparticles is a very challenging but intriguing experimental task.

When the disorder strength grows up the phonon lines start to overlap (see Fig. 4). However, every line can be resolved and the first mode remains well separated. Qualitative change in DOS visible by eye shows up between $S = 0.00024$ and $S = 0.005$. The first mode starts to overlap with its neighbor

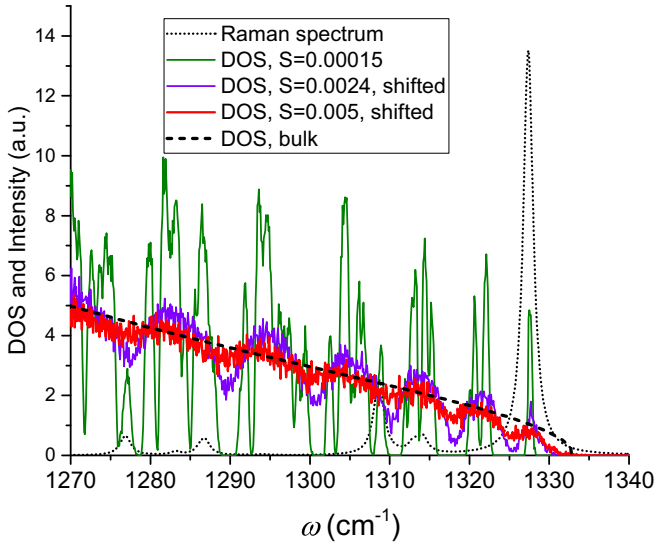

FIG. 4. Phonon density of states vs frequency. The bulk pure DOS is shown by the dashed black curve. The disordered DOS is calculated for a 3 nm spherical diamond particle (about 2450 atoms) with the use of the DMM approach for the weak Gaussian disorder. At small $S = 0.00015$ the DOS has a comblike structure, and the resulting Raman peaks are shown by the dotted black curve. The crossover between the regimes of separated and overlapped levels occurs between $S = 0.0024$ and $S = 0.005$.

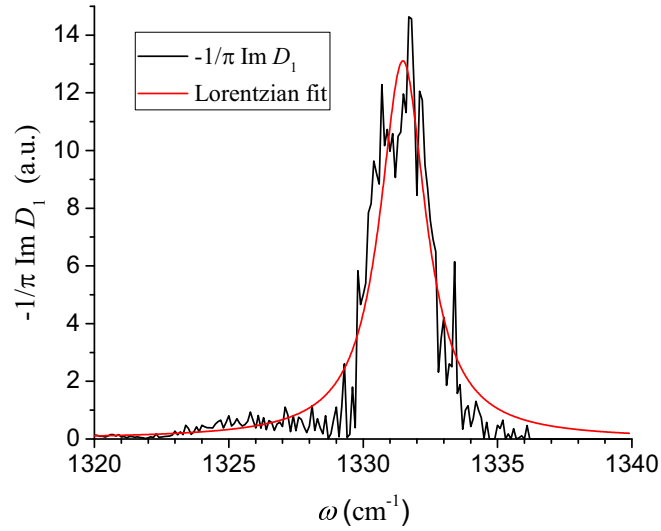

FIG. 5. The spectral weight of the first phonon eigenmode D_1 in a disordered nanoparticle; $S = 0.0024$ and other parameters are the same as in Fig. 4, where this eigenmode is seen as a tiny magenta hump under the Raman peak. Although this value of S is close to the crossover one, the shape of a peak still resembles a semicircle more than the Lorentzian (cf. Fig. 5 of paper I).

whereas the other lines are strongly overlapped and smeared out into the bulklike DOS with some small features on the top. For the stronger disorder the DOS in nanoparticles is almost the same as in the bulk diamond but it has a pronounced tail at $\omega > \omega_0$ hiding the van Hove singularity located at $\omega_0 \approx 1333\ \mathrm{cm}^{-1}$.

The picture described above for the disordered DOS in nanoparticles is in the one-to-one correspondence with the picture of the Raman peak structure in nanoparticles presented in paper I. Indeed, the discrete vibrational eigenmodes (see, e.g., Fig. 5) which we call (not entirely accurately) the "phonons" constitute both the disordered DOS in nanoparticles and the Raman peak (peaks). The only difference is that in the latter case some of these lines are suppressed due to the symmetry properties of related eigenfunctions, and the rest of them are reweighted with the matrix elements of the photon-phonon interaction. These eigenmodes can exist either in the separated or in the overlapped regime depending on the disorder strength and the particle size. Moreover, since the distance from the first triple-degenerate mode to its closest neighbor is larger than any other interlevel spacing in the spectrum the particle can exist in a mixed state (cf. Fig. 4, magenta curve), which provides a *wide* crossover between the purely separated and the completely overlapped regimes.

B. Linewidth and crossover scales

Here we present a comparison between the results of analytical calculations of paper I and the numerics of the present paper concerning the phonon line broadening.

The analytical formula for the phonon linewidth reads

$$\Gamma_n = \omega_n \mu_n(p) \sqrt{S} \left(\frac{a_0}{L}\right)^{3/2} \tag{26}$$

for separated levels, and

$$\Gamma_n = \omega_n \nu_n(p) S \frac{a_0}{L} \tag{27}$$

for overlapped ones. Here $\mu_n(p)$ is the shape p and quantum number n dependent coefficient defined by

$$\mu_n^2(p) = P_p^3 \frac{N}{128} \sum_{l,\alpha} [r(n)_{l,\alpha} r(n)_{l,\alpha}]^2, \tag{28}$$

where P_p converts the linear size of a particle with p facets into the diameter of a sphere L containing the same number of atoms; the sum in Eq. (26) runs over all atoms in a particle. Furthermore, $\nu_n(p) \propto 1/64F$ and strongly depends on the phonon quantum number n. The width of the Raman peak inversely proportional to the particle size has been extracted from the experimental data in Ref. [19], where the particles with $L \sim 10^2$ nm have been analyzed.

First, we test the linewidth dependence on the particle size L predicted by Eqs. (26) and (27). Using the DMM approach and the Gaussian distribution of disorder we investigated numerically the broadening of the first phonon line in spherical diamond particles as a function of the particle size L for two values of the disorder strength parameter S supposedly corresponding to the regimes of separated ($S = 0.0011$) and overlapped ($S = 0.011$) levels. The results are plotted in Fig. 6. We observe the predicted power-law dependencies $\Gamma_1 \propto L^{-3/2}$ and $\Gamma_1 \propto L^{-1}$ for these two cases. Notice that not only the functional dependence of Γ_1 but also the numerical prefactors are in a good agreement with the analytics of paper I.

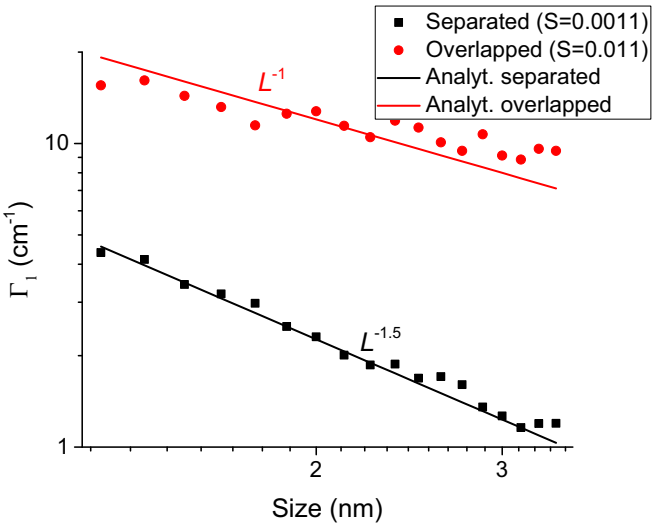

FIG. 6. The broadening parameter for the first optical phonon eigenmode Γ_1 as a function of the particle size L obtained within the DMM-BPM scheme for spherical diamond particles subject to a weak Gaussian disorder. The black squares and the red dots correspond to the disorder strengths $S = 0.0011$ and $S = 0.011$, respectively. The range of L presented in this figure covers the regime of separated levels in the former case and the regime of overlapped levels in the latter one; the lines depict the analytical predictions for these two regimes.

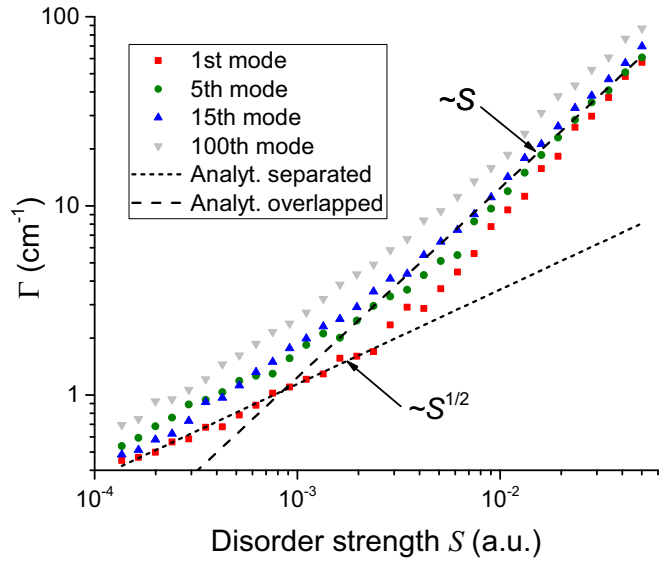

FIG. 7. The broadening parameter Γ_n for several optical phonon eigenmodes as a function of the disorder strength S obtained within the DMM approach for 3 nm spherical diamonds. At small S the regime of separated levels takes place (dotted line), where $\Gamma_n \propto \sqrt{S}$ and reveals a weak quantum number dependence, whereas at larger S the linewidth follows the asymptote $\Gamma_n \propto S$ (dashed line), typical for overlapped levels. The crossover between these regimes occurs at $S \sim 0.005$.

Second, in order to examine the disorder strength and quantum number dependence in Eqs. (26) and (27), we study numerically the broadening parameter Γ_n for several phonon modes with different quantum numbers versus the disorder strength parameter S in spherical 3 nm diamond particles; the method used is the same as for Fig. 6. The result is plotted in Fig. 7. We mention a very good agreement between the numerics and the analytics for the first phonon linewidth Γ_1 including the functional dependence and the crossover scale. For higher modes a transition between the regimes occurs smoother than for the first one manifesting a wider crossover area; for the highest mode, the overlapped regime for all considered S is identified. The tendency for the highest modes to have larger linewidths in the regime of overlapped levels predicted in paper I is correctly reproduced in our numerics; however, we observed that the character of this growth is overestimated by the analytical theory. Nevertheless, the linewidth Γ_n growing with the increase of the quantum numbers n is an important ingredient of our approach. It has been demonstrated in Ref. [45] where the incorporation of this phenomenon essentially improved the χ^2 criterion as compared to the fit with the n-independent linewidth.

Notice that for the fit of Γ_1 on separated levels we used the value $\mu_1 \approx 0.33$ in Eq. (26) which is nearly 1.5 times smaller than its value extracted from the exact DMM eigenfunctions. We attribute this discrepancy to the Lorentz approximation we used in our analytics, whereas the semicircle form (see paper I) gives the additional $\sqrt{3}$ factor which solves the problem. Moreover, it is seen in Fig. 5 that the real phonon spectral weight is not just non-Lorentzian but even asymmetric. We believe that the right-hand side of Eq. (26) should be multiplied by the factor $\sqrt{3}$ caused by an imperfection of the Lorentz approximation.

The third issue we would like to discuss in this subsection concerns the crossover scales between the regimes of the phonon line broadening. The estimates for these scales presented in paper I for the mean particle size L,

$$\mathcal{L}_c \sim \frac{a_0}{S}, \tag{29}$$

at a given disorder strength, and for the disorder strength S,

$$\mathcal{S}_c \sim \frac{a_0}{L}, \tag{30}$$

at a fixed particle size, yield just a qualitative understanding of this issue without answering the question, is this particular phonon mode separated from others or overlapped with them? The answer depends also on the shape and quantum number dependent prefactor omitted in Eqs. (29) and (30). To give some feeling of numbers, we rewrite here the expression for $\mathcal{L}_c$ obtained in the Appendix of paper I for the first vibrational mode of a cubic particle which includes all numerical and parametric prefactors:

$$\mathcal{L}_c = 15\pi^4 F^2 \frac{a_0}{S}. \tag{31}$$

For a diamond, the flatness parameter $F \approx 0.008$, and the prefactor in front of the model-free ratio in Eq. (31) is about 0.094. This means that for a reasonable amount of disorder, say, between $S = 0.001$ and $S = 0.05$, the crossover particle size $\mathcal{L}_c$ varies from $1.9a_0$ to $94a_0$, or, in the metric units, from 0.67 nm to 34 nm. This is precisely the range of parameters intensively studied in the recent experiments. For

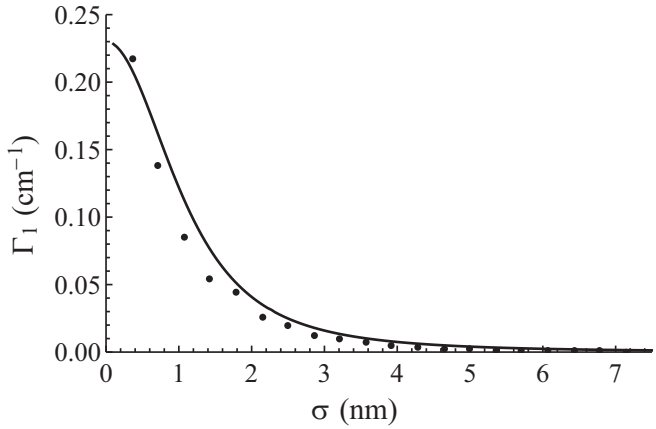

FIG. 8. The damping of the first optical phonon eigenmode Γ_1 as a function of characteristic scale σ of the Gaussian smooth disorder calculated numerically with the use of the EKFG approach (black dots) and analytically (black curve) for cubic particles with $L =$ 8.9 nm. Numerical and analytical results are in a good agreement. For σ comparable with the particle size the broadening is much smaller that for equivalent pointlike impurities. For the highest phonon modes the diminishing takes place at even smaller σ.

nanodiamonds, if one does not account for the adamantane derivatives [64], the lowest reported size is 1.4 nm [23]. Most studies deal with 3–10 nm; we would like to mention here Refs. [20,65–67]. The nanodiamonds of sizes of dozens of nanometers are also actively investigated [10,19,68]. However, at such sizes, the size-quantization-induced Raman peak redshift proportional to L^{-2} becomes lower than the precision of Raman spectrometers; still the broadening effects can stay visible due to L^{-1} dependence in the overlapped levels regime. For other materials, like Si nanoparticles [69] and semiconductor quantum dots [70,71], the sizes from several nanometers to dozens of nanometers are also of highest research interest, which supports the actuality of the considered parameter range.

C. Smooth disorder

In this subsection we discuss the effect of a smooth weak disorder, characterized by the spatial scale σ, on the optical vibrations in nanoparticles.

Utilizing the EKFG approach and studying numerically the Gaussian-correlated disorder introduced in Sec. III D we arrive at the same conclusions as in paper I. Namely, we observe that for a given phonon mode n the broadening essentially depends on the product $q_n\sigma$. When $q_n\sigma \ll 1$ one can use the results for weak pointlike impurities; the smooth character of the disorder provides only small corrections. Notice that for the first phonon mode the condition $q_1\sigma \ll 1$ implies $\sigma \ll L/(2\pi)$ which for nanoparticles of nanometer size means that even the disorder correlated with distances of the order of several lattice parameters leads to the significant suppression of broadening. This statement is illustrated by Fig. 8 depicting the fast decay of $\Gamma_1(\sigma)$ as σ increases observed for cubic particles with $L \approx 8.9$ nm. In the opposite case $q_n\sigma \gtrsim 1$ one observes a drastic diminishing of the damping. This means that in the absence of additional broadening mechanisms this type of disorder is not capable of providing the level overlaps leaving the spectrum in the separated regime.

D. Line shift and mesoscopic smearing

The disorder yields an additional contribution to the broadening of the Raman peak which appears even in the ensemble of *identical* disordered particles due to a "mesoscopic" smearing of phonon lines. The origin of this smearing could be clarified as follows. In the ensemble of identical particles the disorder (say, local mass variations) generates a size-independent shift of the maximal phonon frequency ω_0 proportional to the mean mass variation $\langle\delta m\rangle$ and to the impurity concentration $c_{\rm imp}$. For disorders with zero mean this shift is equal to zero. Nevertheless, even in the latter case there exist the fluctuations of the mean (over the particle) impurity mass value due to the difference of disorder realizations in various particles. This difference generates different fluctuation-induced shifts of ω_0 in particles. Upon the disorder averaging (over an ensemble) these shifts lead to a finite linewidth of the phonon mode as well as to its *size-dependent* shift. The latter shift is nonzero even when $\langle\delta m\rangle = 0$ because it is proportional to the autocorrelator $\langle(\delta m)^2\rangle$, the quantity related to the variance of the function rather to its mean value.

If the disorder realizations in various particles are independent, the above-mentioned fluctuations obey the Poissonian statistics in the discrete ensemble of particles or the Gaussian statistics in the (quasi)continuous one. This smearing mechanism is similar to the smearing that occurs due to the real particle size variation in powders but appears even for identical particles, stemming from the fluctuations of the number of impurities N_i rather than the number of atoms N in a particle.

The above shift is due to (supposedly, independent) fluctuations of disorder. The relative number of atoms participating in a fluctuation is N_i/N and the relative probability of this fluctuation is $1/\sqrt{N_i}$. This yields

$$\Delta\omega_0 \propto \omega_0 \frac{N_i}{N}\frac{1}{\sqrt{N_i}} \propto \omega_0 \frac{\sqrt{c_{\rm imp}}}{L^{3/2}}, \tag{32}$$

which resembles the linewidth behavior for separated levels. In the overlapped regime the levels start to cross-talk, and the analysis becomes more tricky. Evidently, the effect disappears in the bulk limit $N \to \infty$.

Now let us provide some details. In the presence of impurities with concentration $c_{\rm imp} \ll 1$ and masses $m + \delta m$ the average atomic mass in a particle reads

$$\langle m_l\rangle = m + c_{\rm imp}\delta m, \tag{33}$$

while its variance is

$$\langle m_l^2\rangle - \langle m_l\rangle^2 = c_{\rm imp}(\delta m)^2. \tag{34}$$

When calculating how the mass is distributed in a particle containing N atoms, the latter quantity gives the standard deviation

$$\Delta m = \delta m\sqrt{\frac{c_{\rm imp}}{N}}. \tag{35}$$

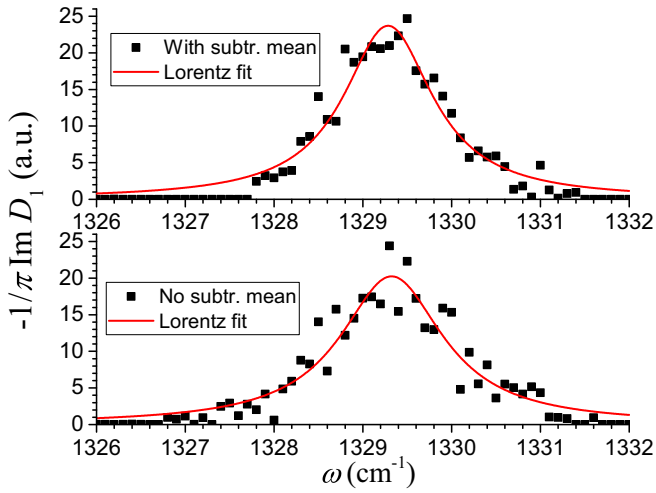

FIG. 9. We investigate the effect of "mesoscopic" smearing examining the linewidth of the first phonon mode Γ_1 for separated levels in 3 nm spherical nanodiamonds with the use of DMM. In the upper panel the Gaussian disorder is forced "by hand" to have zero mean value in each particle separately, which delivers the linewidth $\Gamma_1 \approx 1.2$ cm^{-1}. In the lower panel we did not use that trick allowing the impurity mass to fluctuate from particle to particle. The resulting broadening increases to the value $\Gamma_1 \approx 1.4$ cm^{-1}.

Since ω_0^2 is inversely proportional to the reduced mass of a cell we have the standard deviation of ω_0 in the form

$$\Delta\omega_0 = \frac{\omega_0}{4}\frac{\delta m}{\langle m_l\rangle}\sqrt{\frac{c_{\rm imp}}{N}}. \tag{36}$$

This quantity is simply related to the disorder strength parameter S introduced above:

$$\Delta\omega_0 = \frac{\omega_0}{4}\sqrt{\frac{S}{N}}. \tag{37}$$

Again, we see that the frequency shift given by Eq. (37) is not only proportional to $1/L^{3/2}$ but also depends on other parameters in the same fashion as the linewidth for separated levels. Hence, it should be taken into account. Estimates reveal that it provides about $1/6$ of the overall broadening. For strong disorder and/or overlapped levels this contribution is found to be much smaller.

The above arguments are supported by our numerics. In Fig. 9 we show the difference between the broadening of the first phonon mode Γ_1 in 3 nm spherical diamonds subject to a weak pointlike disorder with and without the subtraction of the mean impurity mass value for every particle. We obtain $\Gamma_1 \approx 1.2$ cm^{-1} for the former case and $\Gamma_1 \approx 1.4$ cm^{-1} for the latter one.

In this section the prediction of paper I for the weak pointlike impurities about the linewidth dependencies $\Gamma_n \propto \sqrt{S}/L^{3/2}$ for separated levels and $\Gamma_n \propto S/L$ for the overlapped ones is verified numerically; the crossover scale typically belongs to the nanometer range. Our numerics confirms a significant diminishing of the damping due to the smooth disorder in comparison with the pointlike one. We also study the "mesoscopic" smearing of the distribution function that occurs even in the ensemble of identical disordered particles.

V. RESULTS: STRONG IMPURITIES

In this section we present the results of numerical modeling for a strong disorder and compare them with the analytical predictions of paper I. In Sec. V A we explain the physical reasons to distinguish between the "weak" and "strong" impurities and outline the results of paper I for the latter. Section V B is devoted to the numerical study of the crossover from the weak to strong regime and to the phenomenon of the resonant scattering. In Sec. V C we observe and investigate a strong dependence of the capability for the impurity to localize the vibrational mode on its location inside the particle, the problem not addressed in paper I because of its analytical complexity. Throughout this section we assume that the disorder is strong if the condition $S \lesssim 1$ is fulfilled but at least one of the requirements, $c_{\rm imp} \ll 1$ or $|\delta m|/m \ll 1$, is relaxed.

A. Preliminary remarks

The weak (and dilute) disorder studied in the previous section is distinguished from other types of disorder by two important features. First, it is sufficient to use as its measure a single small parameter $S \ll 1$ ("disorder strength"). Second, the parameter S is a product of dimensionless impurity concentration $c_{\rm imp}$ and dimensionless randomness parameter (atomic mass, in our case) squared, $(\delta m/m)^2$; both these quantities assumed to be *independently* small, $c_{\rm imp} \ll 1$ and $|\delta m|/m \ll 1$.

When *any* of these parameters becomes of the order of unity, the physical picture changes, even though the smallness of another parameter provides $S \ll 1$. For instance, when $c_{\rm imp}$ becomes of the order of unity (more carefully, when the phonon mean free path $l_{ph} \sim \sqrt[3]{c_{\rm imp}}$ becomes of the order of a few interatomic distances), the approximation of the phonon scattering by the isolated impurities breaks down, and the *multi-impurity* processes which include the interference of the phonon scattering off several impurities come into play. In the lack of a detailed theory we touch this issue slightly detecting the crossover to a novel regime at $l_{ph} \sim 3a_0$ and speculating on general properties of $\Gamma_n(c_{\rm imp})$ for the unitary impurities.

On the other hand, when the variation of the random parameter becomes of the order of its mean value, $|\delta m|/m \sim 1$, or even more, the processes of *multiple scattering off the same impurity* become important, and the parameter S defined above loses its meaning, the results begin to depend on $c_{\rm imp}$ and $\delta m/m$ (more precisely, on U) separately. Moreover, the physics starts to vary with the sign of U: at a positive U (heavy impurities) there is no chance to form a long-lived optical phonon-impurity bound state. On the contrary, at a negative U (light impurities) limited by the condition $\delta m/m \geqslant -1$ (here the equality stands for a vacancy) the impurity scattering is enhanced; it even acquires a resonant character at certain $U_{\rm min}$. For a vacancy we get $U \to -\infty$, and the mass drops out from the result.

Sketching here the analytical results of paper I for the strong disorder, let us mention that the phonon damping Γ_n as a function of the particle size L and the concentration $c_{\rm imp}$ basically follows the same $\sqrt{c_{\rm imp}}/L^{3/2}$ and $c_{\rm imp}/L$ dependencies in the regimes of separated and overlapped phonon

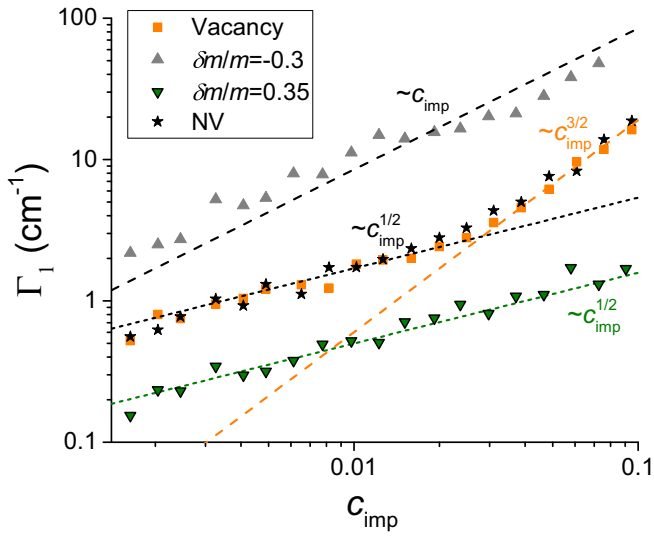

FIG. 10. The linewidth of the first phonon eigenmode Γ_1 versus the impurity concentration $c_{\rm imp}$ for various values of the impurity potential U; the results are obtained numerically for 3 nm spherical diamond particles with the use of DMM. For heavy impurities (inverted green triangles) the broadening follows $\Gamma_1 \propto \sqrt{c_{\rm imp}}$ dependence, whereas light resonant impurities (gray triangles) reveal $\Gamma_1 \propto c_{\rm imp}$ dependence. The vacancies (orange squares) demonstrate a crossover from the square-root dependence to the new regime $\Gamma_1 \propto c_{\rm imp}^{3/2}$ at higher concentrations. The NV centers (black stars) behave similarly to the vacancies.

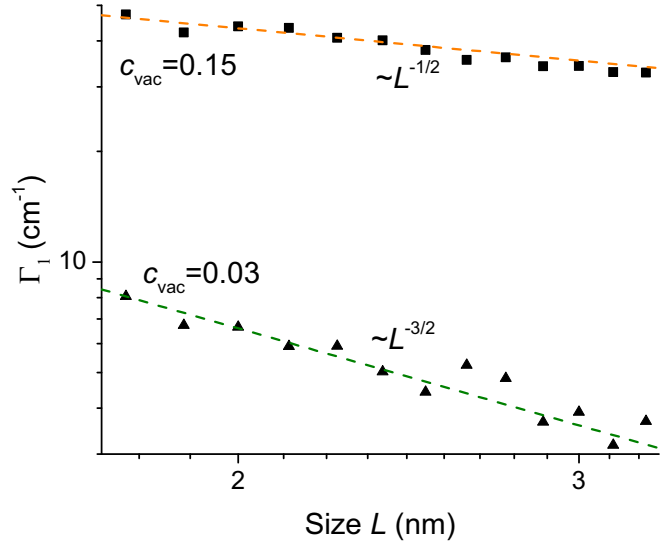

FIG. 11. The linewidth of the first phonon eigenmode Γ_1 as a function of the particle size L calculated numerically with the use of DMM for spherical diamond particles and for the impurities in the form of the empty vacancies. The plot is presented for two values of the vacancy concentration corresponding to the "dilute" and to the "dense" regimes wherein the linewidth behaves as $\Gamma_1 \propto \sqrt{c_{\rm imp}}/L^{3/2}$ and $\Gamma_1 \propto c_{\rm imp}^{3/2}/\sqrt{L}$, respectively.

levels which it demonstrates for the weak disorder. The only difference occurs in the proximity of the resonance wherein an appearance of the long spatial scale ζ leads to the crossover in the L dependence taking place at $L \sim \zeta$. Furthermore, the capability of a strong light impurity to capture the phonon and the frequency of the impurity-phonon bound state evaluated analytically depend on the parameter ζ but not on the location of the impurity.

B. Strong impurities and NV centers

The numerically calculated phonon linewidth of the first vibrational mode Γ_1 as a function of the impurity concentration $c_{\rm imp}$ is depicted in Fig. 10 for several values of the parameter U (or $\delta m/m$), namely, (i) for moderately heavy impurities with $U \approx 0.23$ ($\delta m/m \approx 0.35$) by the inverted green triangles; (ii) for the resonant impurities with $U \approx -0.43$ ($\delta m/m \approx -0.30$) by the gray triangles; (iii) for the empty vacancies, which corresponds to the unitary limit $U \to -\infty$ ($\delta m/m \to -1$) by the orange squares; and (iv) for the NV centers described as a vacancy plus the neighboring heavy impurity with $U \approx 0.14$ ($\delta m/m = 0.17$) by the black stars. We observe that in the considered range of concentrations heavy and light (resonant) impurities lead to the dependencies peculiar for separated ($\Gamma \propto \sqrt{c_{\rm imp}}$) and overlapped ($\Gamma \propto c_{\rm imp}$) regimes, respectively, which is not a surprise because the theory predicts for resonant impurities the strong enhancement of the prefactor (also seen in Fig. 10) capable of transferring the system from one regime to another even though the concentration $c_{\rm imp}$ and the absolute value of the mass defect $|\delta m/m|$ are not very different in these cases.

We observe another interesting phenomenon for the unitary impurities and for the NV centers. As we know from the analytics (see also below) the U dependence disappears in the unitarity. Moreover, in Fig. 10 the crossover from the square-root $c_{\rm imp}$ dependence of separated levels to yet another regime $\Gamma_1 \propto c_{\rm imp}^{3/2}$ is seen at high concentrations. This regime is not predicted by our analytics in paper I. Notice that the crossover takes place at $c_{\rm imp} \simeq 0.03$ which presumably coincides with the boundary between the "dilute" and the "dense" regimes for the phonon mean free path l_{ph}, where the multi-impurity physics begins to be important.

In order to cross-check our understanding of the crossover for $\Gamma_1(c_{\rm imp})$ depicted in Fig. 10 we calculate numerically the $\Gamma_1(L)$ dependence for the vacancies (see Fig. 11). We observe that in the regime when $\Gamma_1 \propto \sqrt{c_{\rm imp}}$ its size dependence is $\Gamma_1 \propto 1/L^{3/2}$, in agreement with our analytics for separated levels. In the novel "dense" regime $\Gamma_1 \propto c_{\rm imp}^{3/2}$ it behaves as $\Gamma_1 \propto 1/\sqrt{L}$ yielding

$$\Gamma_1 \propto \frac{c_{\rm imp}^{3/2}}{\sqrt{L}}. \tag{38}$$

Inspecting all formulas for Γ_n we discover that each power of concentration always comes with the first power of the mean particle size, i.e., as a product $c_{\rm imp} \times L$.

At the moment, we have no detailed theory for the behavior given by Eq. (38) although the underlying physics is evident. Below we just speculate about the *binary* disorder which is invariant under the duality transformation $c_{\rm imp} \Longleftrightarrow 1 - c_{\rm imp}$. More accurately, the duality condition requires for physical observables the symmetry property (cf. Ref. [72])

$$M_1^A M_2^B \mathcal{G}(c_{\rm imp}) = M_2^A M_1^B \mathcal{G}(1 - c_{\rm imp}), \tag{39}$$

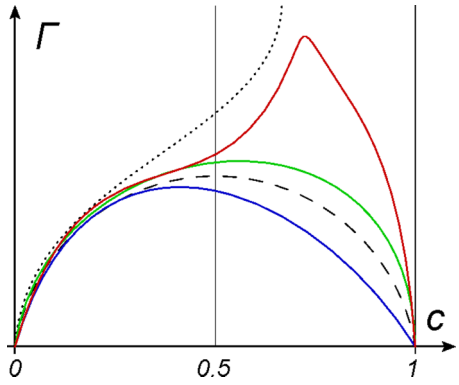

FIG. 12. The phonon linewidth Γ plotted versus the impurity concentration c: a schematic plot in the entire interval of $c \in [0, 1]$ for the binary disorder; all the curves are normalized to the mass of the "first" material. Blue and green curves depict the situations when the "impurities" are just slightly heavier and lighter than the host material, respectively, and the black dashed line represents their separatrix $\sqrt{c(1-c)}$. Black dotted line portrays the percolation transition that occurs in the unitary limit $U = -\infty$, and the red one shows Γ close to the criticality, i.e., for the very light "impurity" atoms.

where M_1 and M_2 are the masses of atoms of the first and second sort, respectively, while A and B are certain exponents (which may coincide or be equal to zero for some quantities) specific for any observable. Transferring all the mass dependence to the right-hand side of Eq. (39) we get

$$\begin{aligned} \mathcal{G}(c_{\text{imp}}) &= \mathcal{G}(1-c_{\text{imp}})(1+\delta m/m)^{\alpha} \\ &\approx \mathcal{G}(1-c_{\text{imp}})(1+\alpha\,\delta m/m), \end{aligned} \tag{40}$$

where $\alpha = A - B$, and the approximate equality in Eq. (40) holds for small $\delta m/m$. Thus, we obtain that any mass-dependent observable (including the broadening parameter Γ_n) is not simply a subject of the duality condition $c_{\text{imp}} \Longleftrightarrow 1 - c_{\text{imp}}$ but should be simultaneously reweighted with some mass-dependent prefactors.

The behavior of $\Gamma(c_{\text{imp}})$ in the entire interval of concentrations $0 < c_{\text{imp}} < 1$ is schematically plotted in Fig. 12. It is assumed that the region of small $c_{\text{imp}} \ll 1$ corresponds to a small number of impurities with mass M_2 and a material with mass M_1, which forms the host lattice there, while the region where $c_{\text{imp}} \simeq 1$ describes the opposite situation. The entire picture is normalized to the first mass so the mass of the second element is treated as light or heavy relative to the first one. The linewidth dependence on the parameter c_{imp} for second atoms slightly heavier and slightly lighter than the first ones is depicted in Fig. 12 by the featureless blue and green curves, respectively. Both of these curves behave as $\sqrt{c_{\text{imp}}}$ near zero and as $a\sqrt{1-c_{\text{imp}}}$ near unity, where a is some mass-dependent prefactor [cf. Eq. (40)] with $a < 1$ for heavy M_2 atoms and $a > 1$ for light M_2 atoms. We match these asymptotes at intermediate concentrations following the continuity reasons. With the increasing of the second mass the blue curve in Fig. 12 does not change drastically; its right shoulder continues to decrease monotonically. This is not the case for the light M_2 atoms. To understand this better consider the extreme case of vacancies when M_2 is equal to zero and the impurity potential U reaches the unitary limit becoming the infinite pointlike on-site repulsion. The appearance of such on-site potential means the elimination of this site from the lattice dynamics. When the number of eliminated sites is small, they work as the conventional strong impurities; however, at certain critical concentration c_{cr} they lock the propagation of vibrational modes. The transition occurs according to the percolation scenario (notice that the particle diffusion and the propagation of vibrational modes on fractals belong to the same universality class; see Ref. [73]). It is natural to assume that the phonons become poorly defined (overdamped) excitations before they die; i.e., the phonon rate is the critical quantity in this problem:

$$\Gamma \propto (c_{\text{imp}} - c_{cr})^{-\tau}, \tag{41}$$

with $\tau > 0$ being some percolation-related critical exponent. The behavior of Γ in the unitary limit is shown in Fig. 12 by the dashed black line, with the square-root increase at small concentrations crossing over to the critical behavior near the percolation transition. Finally, the red curve in Fig. 12 represents the c_{imp} dependence of Γ for light M_2 atoms close to unitarity. It is drawn based on the continuity arguments as an interpolation between the regimes described by the green and the dotted black curves, and it includes the region near c_{cr} wherein the damping of phonons (or, probably, already "phasons"; see [73]) reveals the critical properties, although the real localization of vibrational modes does not take place yet.

The important feature common for the vacancies and for very light M_2 atoms is an inflection point on the left shoulder of the $\Gamma(c_{\text{imp}})$ dependence stemming from the necessity to match the square root and the critical asymptotes. Although our methods are not well suited for the treatment of the phonon modes at intermediate impurity concentrations ("dense" regimes), we believe that the departure from the $\sqrt{c_{\text{imp}}}$ low-concentration dependence of Γ to the more fast $c_{\text{imp}}^{3/2}$ behavior seen in Fig. 10 for two numerical plots related to the light impurities (NV centers and vacancies) revealing this inflection is a strong argument in favor of the picture we presented above based on general arguments.

C. Resonant scattering and localized states

It was predicted in paper I that the damping of phonons grows essentially as a function of U in the vicinity of its resonant value determined from the condition for the relevant spatial scale

$$\zeta = \frac{\pi}{2q_D}\left(1 + \frac{8\pi^2 F}{q_D a_0 U}\right)^{-1} \tag{42}$$

to diverge. It occurs at

$$U_{\text{min}} = -\frac{8\pi^2 F}{q_D a_0}, \tag{43}$$

where q_D is the Debye momentum. In Fig. 13 we plot the analytical curve for the linewidth of the first phonon mode Γ_1 as a function of $\delta m/m$ at $c_{\text{imp}} = 0.02$ (black line) and compare this plot with Γ_1 calculated numerically within the scheme presented in Secs. II and III of this paper (black dots).

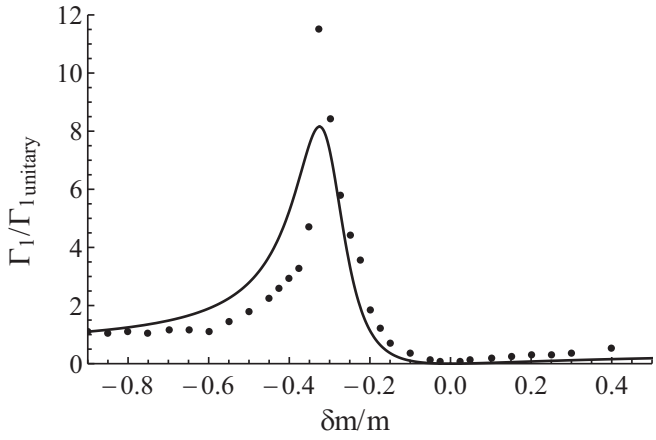

FIG. 13. The linewidth of the first optical phonon mode Γ_1 normalized to its unitary value as a function of $\delta m/m$ at the fixed concentration of strong impurities $c_{\rm imp} = 0.02$ calculated numerically for 3 nm diamond particles with the use of DMM (dots) and analytically using the T-matrix approach (line). For $\delta m/m \to -1$ ($U \to -\infty$) (vacancies) and for $\delta m/m \to +\infty$ ($U \to 1$; extremely heavy impurities) the linewidth saturates at different values. At $\delta m/m \approx -0.30$ ($U \approx -0.43$) the damping acquires the resonant character.

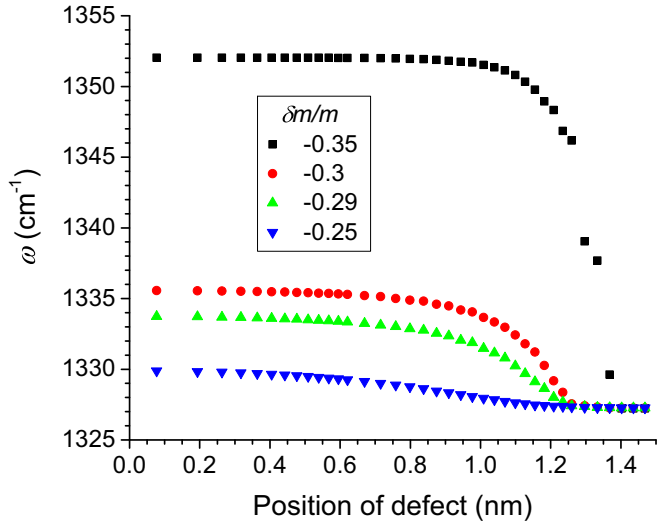

FIG. 14. The highest phonon frequency in a particle versus the position of a single impurity of given mass calculated numerically for 3 nm spherical diamond particles with the use of DMM. When the frequency is higher than $\omega_0 = 1333\ {\rm cm}^{-1}$ the corresponding vibrational mode is localized on the impurity. The maximal phonon frequency decreases when the distance between the location of the impurity and the center of a particle grows. It leads to the absence of localization if the defect is close enough to the particle boundary.

We use q_D as an adjustable parameter to tune the maximum of the analytical curve to coincide with the maximum in our numerics (for the reason to do this see paper I) which happens at the reasonable value $q_D \approx 0.47\pi/a_0$ yielding $(\delta m/m)_{\rm min} \approx -0.30$ ($U_{\rm min} \approx -0.43$). We see that the analytical theory underestimates the effect. This is expected because the T-matrix approximation we used only manifests the phenomenon while for its detailed treatment the specific methods adopted to deal with the resonant scattering are required. For light impurity atoms with $\delta m/m < -0.7$ ($U < -2$) and for heavy ones with $\delta m/m \to +\infty$ ($U \approx 1$) the damping Γ_1 obtained numerically saturates at different values in accordance with the analytical predictions. Generally, we report a good *qualitative* agreement in the description of the resonant features between the analytics of paper I and the numerics of this paper. Notice that we presented the resonant behavior in Fig. 13 in terms of $\delta m/m$ instead of U because it looks more evocative.

Now we shall analyze a possibility to localize the vibrational mode on the impurity. The energy of this state ω_{loc}, slightly exceeding the maximal energy of the optical phonon ω_0, is found to be (see paper I)

$$\omega_{\rm loc} = \omega_0[1 + F(a_0/\zeta)^2]. \tag{44}$$

We model the single-impurity problem investigating numerically 3 nm spherical diamond particles by means of DMM. We obtain a very interesting new phenomenon which has not been predicted by the analytical theory of paper I. Namely, we find that the capability for the impurity to localize the phonon strongly depends on the location of this impurity inside the particle: it is maximal at the particle center and rapidly decays to the boundary.

Our argument in favor of this picture is presented in Fig. 14 where we plot the maximal phonon frequency as a function of the distance from the defect to the particle center for several nearly resonant values of the impurity potential U. One can see that if the localized state emerges ($U_{\rm min} > U$) then its frequency is almost constant as long as its wave function does not "feel" the boundary (see Fig. 15). When the defect is near the boundary, $\omega_{\rm loc}$ decreases and the localized state disappears. It occurs because the amplitudes of optical vibrations near the boundary are much smaller than at the center, and the impurity cannot "catch" the phonon which results in the usual scattering rather than in the localization of the vibration.

In Fig. 15 we portray the wave function for the highest phonon mode in the localized regime $U_{\rm min} > U$ for two particular cases, namely when the same impurity is located at the center of the particle [panel (a)] and when it lies near its boundary [panel (b)], thus visualizing the above reasoning. We see that in the former case the wave function is concentrated in the closest vicinity of the defect, the decay rate being much shorter than the particle size which reflects the phonon localization. On the contrary, if we settle down the impurity near the particle boundary, the phonon wave function is smeared over the particle which implies an extended state. Moreover, the wave function in the latter case resembles the pure case (cf. Fig. 3 of Ref. [34]); the only impurity-induced disturbance is seen in the neighborhood of the impurity.

To summarize, we find numerically that the regimes of separated and overlapped levels observed for the phonon linewidth in a weakly disordered particle survive for the strongly disordered dilute case. Inspecting the line broadening due to vacancies and NV centers at yet higher concentrations we identify a crossover to the novel regime $\Gamma \propto c_{\rm imp}^{3/2}/\sqrt{L}$ attributed to the multi-impurity scattering in the proximity of the percolation transition. Our numerics qualitatively confirms all analytical results for the resonant phonon scattering including

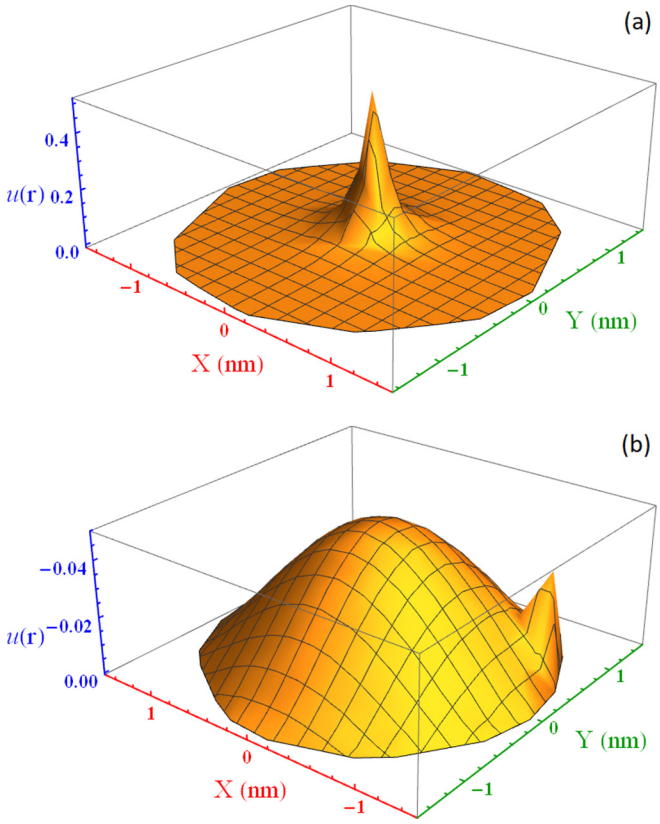

FIG. 15. The phonon wave function obtained numerically for 3 nm spherical diamonds using DMM. Two different locations of the impurity with $\delta m/m = -0.33$ are studied. When the defect lies near the particle center the highest in energy vibrational mode is localized (a), whereas the impurity settled near the boundary leads to the wave function resembling the pure case with some local feature around the defect (b).

the formation of the phonon-impurity bound state which is found to be dependent on the impurity location inside the particle.

VI. RESULTS: SURFACE CORRUGATIONS

In this section we present our results concerning the influence of several types of realistic surface disorder on the broadening of the volume optical phonon modes which contribute to the Raman spectrum of nanoparticles.

Below we are interested in the effect of *surface* (i.e., two-dimensional or quasi-two-dimensional) irregularities on the behavior of *volume* (i.e., three-dimensional) excitations (volume phonons). Surely, both propagating surface modes (surface phonons) and surface-volume mixed modes (breathers, etc.) exist and play an important role in the physics of nanoparticles. Moreover, the approaches we developed in the present work are also applicable for a treatment of these modes. However, the characteristic frequencies of the surface modes lie away from the frequency range relevant for the main Raman peak. Therefore, we postpone their investigation for the future.

When investigating the surface corrugations, we observe only a minor influence of this type of disorder on the broadening of the first phonon mode as compared to the volume disorder considered in previous sections, the statement valid for both the "peeled apples" and "nibbled apples" models we studied. Even for the strongest disorder we get $\Gamma_1 < 1$ cm^{-1}. In Fig. 16 we plot the broadening parameter Γ_1 versus the impurity concentration $c_{\rm imp}$ within the framework of the nibbled apples model. The volume of a particle is taken clean, and the surface disorder fails to overlap the first level with its neighbor. This leads to the square-root dependence of the linewidth on the impurity concentration seen in Fig. 16, which agrees with the prediction of paper I for separated levels. Notice that the notion of concentration should be revised for the surface impurities. Say, for the nibbled apples one should count the number of "jobbsings" (removed bits) and then divide it by the total number of surface bricks, whereas for the peeled apples which could be regarded as a convex irregular polyhedra the definition of concentration includes the average distance between the ribs in the disordered particle divided by the same quantity in the pure one.

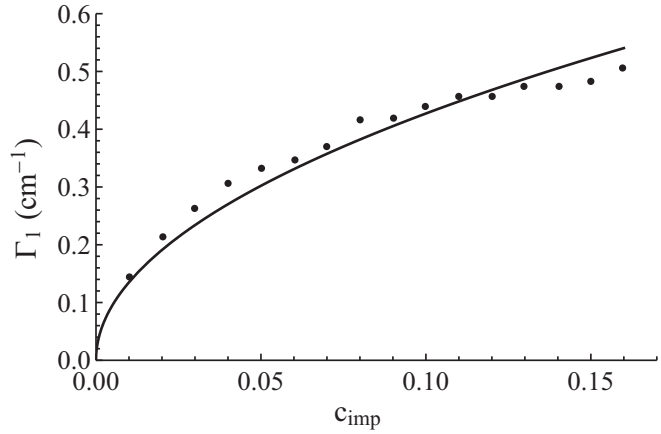

FIG. 16. The linewidth of the first phonon line Γ_1 as a function of the surface impurity concentration $c_{\rm imp}$ calculated with the use of the EKFG approach for 4.5 nm diamond particles within the model of nibbled apples. The numerical results (dots) are well described by the square-root dependence (line).

The importance of the surface disorder increases for higher phonon levels where the notion of classical chaos is better applicable since $1/n$ is a version of the quasiclassical parameter. For the highest modes the (almost) classical chaotization due to the surface roughnesses works better resulting in the overlapped regime at the same number of impurities which did not allow the lowest levels to overlap (see Fig. 17). We conclude that the surface corrugations may slightly affect the main Raman peak only on its left shoulder; the scattering by the volume impurities remains the dominant broadening mechanism in nanoparticles.

Another feature of the surface disorder which makes it less important than the volume one is the rapid decay of its contribution to Γ_n with L increasing. We shall demonstrate it considering the nibbled apples model as an example. This model allows two modifications: for one of them the size of jobbsings is scaled with the particle size and for another one it does not, so for very large particles the impurities acquire a truly surface pointlike character.

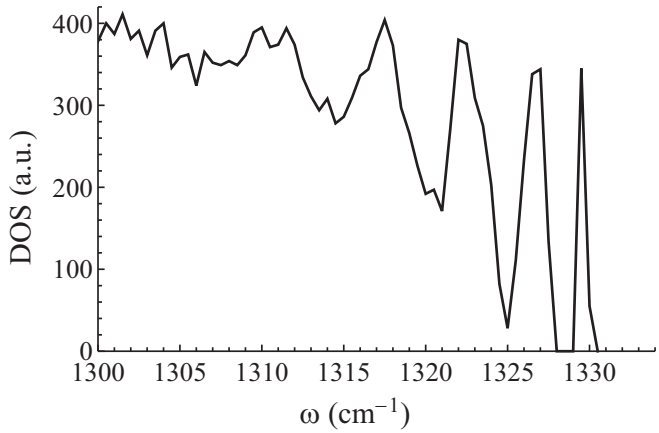

FIG. 17. The DOS function calculated numerically for disordered 4.5 nm diamond particles with the use of the EKFG approach within the peeled apples model (result for the nibbled apples is very similar). Several lowest phonon levels are separated whereas the higher levels overlap due to the same amount of the surface disorder.

In the former case the dependence $\Gamma_n(L)$ could be obtained from the scaling arguments. Inspecting the EKFG equations we observe that due to the (statistically understood) scale invariance of the disordered EKFG problem with this type of imperfection its eigennumbers scale in the same manner as for the pure EKFG problem [34]:

$$q_n^2(L_1)L_1^2 = q_n^2(L_2)L_2^2. \tag{45}$$

Thus, the ensembles of particles of different sizes are similar to each other, and the corresponding broadenings are mutually related by the scaling law

$$\Gamma_n(L_1)L_1^2 = \Gamma_n(L_2)L_2^2 \Longleftrightarrow \Gamma_n(L) \propto \frac{1}{L^2}. \tag{46}$$

We argue that this $\Gamma_n \propto 1/L^2$ dependence is the slowest size dependence possible in both models of surface corrugations (at least, for the separated phonon modes). Qualitatively, it can be understood as follows. Let us inspect the Born impurity scattering on the separated levels [see Eq. (29) of paper I]. The squared linewidth parameter Γ_n is proportional to the fourth power of the phonon wave function $Y_n \propto 1/\sqrt{N}$. Let us introduce L_d as the characteristic scale of the surface disorder. Then each of four wave functions provides the factor $(L_d/L)/L^{3/2}$ and the surface area where the interaction with disorder occurs is estimated as $c_{\rm imp}L^2$. This yields $\Gamma_n^2 \propto L_d^4/L^8$. If now L_d scales as the particle size, $L_d \propto L$ (the first modification of the nibbled apples model), then we get $\Gamma_n \propto 1/L^2$. If however the surface disorder is not scaled with the particle size, $L_d \propto$ constant (the second modification), we obtain $\Gamma_n \propto 1/L^4$. An intermediate situation $L_d \propto L^\beta$ with $0 < \beta < 1$ yields $\Gamma_n \propto 1/L^{4-2\beta}$. The general reason for these rapid decay laws is that the phonon wave function in the disordered region near the surface tends to zero (cf. with the position-dependent localization in Sec. V C). For disorders scaled slower than L the relative volume of the disordered region decreases when the particle grows. This results in a faster decay of the scattering amplitude.

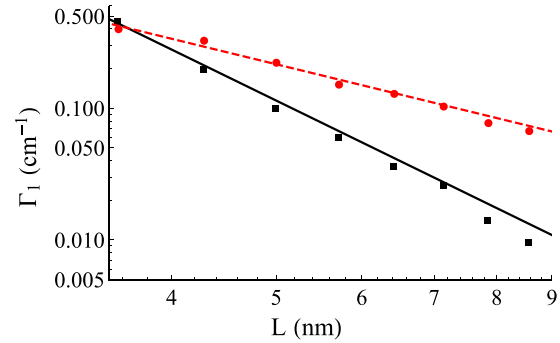

FIG. 18. The linewidth of the first optical phonon mode Γ_1 versus the particle size L calculated numerically for the model of nibbled apples with the use of the EKFG method at the surface impurity concentration $c_{\rm imp} = 0.1$. The red dots correspond to the scaled disorder and the black squares correspond to the unscaled one; the lines depict $1/L^2$ and $1/L^4$ dependencies, respectively.

This is exactly what we observe in our numerics. The result is depicted in Fig. 18, where $1/L^2$ and $1/L^4$ regimes are found for Γ_1 calculated for the nibbled apples model in its scaled and unscaled modifications, respectively.

Thus, the surface corrugations yield a minor input to the broadening of phonon levels for the volume optical phonons as compared to the volume disorder. This is caused by the vanishing of the phonon wave function on the particle surface.

VII. DISCUSSION AND CONCLUSIONS

In this concluding section we summarize the outcome of the numerics reported in paper II and compare them with the results of the analytical consideration of paper I in Sec. VII A. Possible applications and generalizations of our theory as well as its disadvantages and limitations are discussed in Sec. VII B.

A. Summary

Both papers I and II constituting the present work are devoted to the treatment of disorder influence on the propagating optical vibrational modes in powders of nanoparticles of nonpolar crystals considering the diamond particles as a representative example. The linewidths and the line shifts of these phonon modes as well as the shapes of individual spectral lines in the phonon spectra are investigated as functions of the mean particle size, the particle shape, the impurity concentration, the strength and the type of disorder, and the phonon quantum number, addressing these issues analytically in paper I and numerically in the present paper. Furthermore, we apply our knowledge of this subject for the analysis of the structure of the main Raman peak, in view of the possibility of extracting confidently the values of the above-mentioned parameters from the experimental data [45].

In both papers we apply the methods of treatment we developed previously for pure nanoparticles in Refs. [33,34], utilizing the discrete atomistic approach in the form of the DMM-BPM method and the continuous elasticity-theory-like approach solving the EKFG equation with the Dirichlet boundary condition, depending on the particular problem at

hand. Parameters emerging in our approaches are simply related to the parameters of microscopic models of solids, i.e., of the Keating model. We properly adopted both methods for the analytical calculations in paper I and for the numerical ones in paper II.

As far as the disorder is concerned, we investigated several types of imperfections most interesting from theoretical and experimental points of view. In paper I we studied analytically weak Gaussian disorder in its pointlike and smooth modifications and strong binary disorder, both considered in the regime of "dilute" concentrations. In paper II we had two objectives, namely to check numerically the predictions of the analytics and to investigate realistic regimes of disorder hardly analyzable analytically. Executing the second task we studied the disorder at the intermediate impurity concentrations and at an arbitrary disorder strength as well as in two models of surface corrugations. We also investigated the isotopic impurities and the NV centers (nitrogen plus vacancy) widespread in diamonds.

The main observation of paper I is the existence of two regimes of behavior for the phonon linewidth Γ_n depending on the particle size and the impurity strength investigated. For the smallest particles and/or for the weakest disorder the phonon levels are separated. This results in $\Gamma_n \propto \sqrt{S}/L^{3/2}$ dependence on these parameters; the prefactor varying with the particle shape and with the phonon quantum number could be calculated either analytically or numerically. When the particle size and/or the strength of disorder increases the levels start to overlap, and the linewidth crosses over to another regime $\Gamma_n \propto S/L$ with different quantum number and shape dependent prefactor.

Investigating numerically weakly disordered particles we confirm the analytical predictions of paper I. For the pointlike impurities we demonstrate the regimes of separated and overlapped levels and reproduce the dependencies $\Gamma \propto \sqrt{S}/L^{3/2}$ for the former and $\Gamma \propto S/L$ for the latter regime, respectively. We slightly correct the numerical prefactor in the former case and attribute this correction as a certain disadvantage of the Lorentz approximation. We observe that the rapid growth of the linewidth as a function of quantum number predicted by the analytical theory of paper I overestimates the effect which nevertheless exists and is found to be important for the fit of experimental data. We estimate the crossover scales between the regimes and obtain that for the realistic values of the disorder it lies on the scale of nanometers or dozens of nanometers for the mean particle size L, i.e., in the most intensively studied and most interesting range of parameters. Considering the case of a smooth random potential we inspect and confirm numerically a significant decrease of the linewidth when the characteristic spatial scale σ of the potential grows toward the particle size L. We also address (both analytically and numerically) an issue which has been only slightly touched on in paper I discussing the phenomenon of mesoscopic smearing of the distribution function which is predicted to arise in the ensemble of disordered particles due to the variations of disorder realizations in various particles and to survive even in the ensemble of identical in size and shape particles.

We examine numerically the phonon line broadening in the regime of strong rare impurities when the parameter S loses its meaning and the disorder is characterized by two independent quantities such as the dimensionless impurity potential U and the dimensionless impurity concentration $c_{\rm imp}$, allowing the potential U to be strong enough, $|U| \gtrsim 1$, and mostly keeping the concentration dilute, $c_{\rm imp} \ll 1$. We find that the regimes of separated and overlapped levels with their characteristic $c_{\rm imp}$ and L dependencies survive for strongly disordered particles as well, although the crossover between these regimes could be shifted due to the large U-dependent prefactor. For vacancies and NV centers we discover a crossover which occurs at some intermediate concentration to the regime with $c_{\rm imp}^{3/2}/\sqrt{L}$ dependence of the linewidth not appearing in the low-$c_{\rm imp}$ theory of paper I. This stems from the multi-impurity scattering processes ("dense" defects). We also argued that for the binary disorder the above-mentioned dependence [more accurately, existence of an inflection point in the $\Gamma_n(c_{\rm imp})$ dependence] emerges for the light enough impurities reflecting the proximity to the percolation transition taking place in the unitary limit, and qualitatively restore the behavior of $\Gamma_n(c_{\rm imp})$ in the entire interval $0 < c_{\rm imp} < 1$.

When examining the resonant enhancement of the phonon damping, we observe a good qualitative agreement between the analytical approach and the numerical calculations. Although the former underestimates the amplitude of the effect, it qualitatively reproduces all principal features of the behavior of the damping Γ_n as a function of its parameters. We report the similar agreement for our numerical study of the phonon localization by a strong light impurity. The novel phenomenon not predicted analytically and investigated only by the numerical tools in the present paper is the strong dependence on the location of impurity inside the particle observed for the capability of the impurity to localize the phonon: this capability is maximal when the defect is located in the center of a particle and decays rapidly when it moves toward the boundary.

We inspect how the surface corrugations affect the linewidths of volume (optical) phonons studying numerically two models of the surface disorder named the peeled apples model and the nibbled apples model. For the reasonable values of parameters we found that the surface contribution to the damping is essentially smaller than the contribution of the volume disorder. Since the effect is small we concentrated mainly on the regime of separated levels. The linewidth of the main phonon mode Γ_1 as a function of the surface impurity concentration is shown to behave similarly to the volume impurities, whereas the linewidths of the highest phonon modes grow rapidly due to their better chaotization. The phonon linewidth decays with an increase of the particle size faster than it occurs for the volume impurities as a result of the rapid decrease of phonon wave functions on the surface. The character of this decay is estimated analytically and calculated numerically as $\Gamma_n \propto 1/L^2$ for the disorder scaled with the particle size and as $\Gamma_n \propto 1/L^4$ for the unscaled imperfections.

We monitored numerically the asymmetry of phonon lines and their non-Lorentzian shape predicted in paper I.

We conclude that the analytical theory of paper I is verified and approved by the numerics of paper II; the minor deviations caused by an approximate character of the analytical approach could be easily corrected. Furthermore, the

numerical methods formulated in paper II allowed us to study the regimes which are hardly achievable analytically but interesting from the experimental point of view.

B. Discussion and prospects

The present paper continues our efforts to build up a new microscopic theory of Raman scattering in nanopowders of nonpolar crystals started in Refs. [33,34,44,45]. We believe that this theory should replace in usage the phonon confinement model previously applied for the analysis of Raman spectra of nanoparticles. Starting from the microscopic quantum description of mechanical vibrations in the finite-size systems and incorporating the photon-phonon interaction under the assumption (obviously valid for nonpolar crystals) that the polarization of a solid occurs exclusively due to the atomic displacements, this theory, being applied for the interpretation of existing experimental data, is able to provide us with the most complete information about the physical parameters of a powder, about the shape and the structure of particles constituting the powder, and about the collective excitations that govern the atomic dynamics in particles.

All this could be done with an accuracy limited only by the accuracy of Raman (optical and therefore precise) experiment. The fit of the Raman experiment performed in Ref. [45] where four parameters of the nanopowder have been confidently extracted from the data clearly demonstrates significant increase of the precision when the data are evaluated within the framework of our method as compared to the PCM approach; the latter is shown to work worse and worse for smaller particles.

In addition, the PCM is in fact a purely phenomenological approach which simply replaces the bulk result by a convolution of the bulk result with a certain inexplicable Gaussian, with the further assignment for the Gaussian-caused decay rate of a phonon spectral weight the meaning of a particle size. Meanwhile, it has been shown in Ref. [33] that the microscopic theory (in its approximate version) allows the formulation in terms of a convolution of bulk formulas; however, the function convoluted with the bulk DOS has nothing in common with the Gaussian. That is why we believe that several attempts made recently in order to cure the PCM are doomed at best to partial success. On the contrary, the significant increase in the accuracy of the data interpretation promised by the present approach is of paramount importance for the industrial manufacturing of nanoparticles as well as for their scientific and technological employments.

The only imperfection of this theory in comparison with the PCM is its relative complexity. Indeed, since even the eigenfrequency of the main phonon mode was shown to be 20% varying with the particle shape [34], both the DMM-BPM and the EKFG methods require the numerical calculations (not very tedious, though) for any particle shape beyond the minimal set of a cube, sphere, and cylinder. To make the things easier, we plan a paper revisiting the existing data with the use of our theory and containing step-by-step description of programming operations which would simplify the life of possible exploiters.

Although the main principles of this theory are elaborated, many important problems still remain to be solved. Let us outline some of them. As far as the Raman experiment in the nanopowders is concerned, it would be very interesting to extend the theory to elongated particles and to the closely related problem of nanopowders with multiparametric distribution functions. Furthermore, in the present research we concentrated on the intrinsic for nanoparticles mechanisms of disorder. Investigation of such extrinsic mechanisms of the optical phonon line broadening as a solvent or crystalline matrix impact as well as a contact with other particles in a powder are of high interest. Next, an extension of the continuous EKFG treatment onto the anisotropic crystals requires a more sophisticated tensor modification of the EKFG method itself. Moreover, the analysis of Raman scattering in the polar crystals within the framework of the same theory as done for the nonpolar ones would essentially extend the range of applicability of the theory. An experimental search and a proper theoretical description of the surface (surface phonons) and surface-bulk mixed (i.e., breathing) modes in nanoparticles which should create their own Raman peaks is one more task for our method; the latter phenomena might be very helpful for testing the nanoparticle surface.

Considering possible extensions and generalizations of the theory of the optical phonon line broadening in particles not necessarily appealing to the Raman experiment we should mention an intriguing task to include in the theory the anharmonicity-induced processes of inelastic phonon scattering by each other which would lead to a temperature dependence of the phonon linewidth (by the way, seen also in the Raman experiment [74]). In the meantime, the lifetimes of optical phonons (stemming from both inelastic and elastic processes) are a subject of extensive experimental investigation in other confined systems such as quantum dots and short nanotubes. Our treatment of the elastic phonon rates adjusted for the Raman experiment in nanoparticles could be applied for these systems without a significant revision. Moreover, it could be applied also for the treatment on these rates in the *polar* nanocrystals as far as other experimental setups different from the Raman experiment are involved.

Addressing possible generalizations of the present theory for the Raman processes due to different (nonphonon) excitations one should mention first the case of strongly disordered (probably, amorphous) particles where the notion of propagating phonon modes is meaningless, and the vibrational dynamics is due to the "fractons" [73], which is an issue requiring quite a different analytical approach as compared to the one used in the present work. Finally, it would be very beneficial to develop an EKFG-like theory for the Raman (or Mandelstam-Brillouin) scattering due to magnons in the magnetically ordered particles wherein the Bloch equations should replace the phonon equations of motion.

ACKNOWLEDGMENT

The authors are thankful to Igor Gornyi for valuable comments. This work is supported by the Russian Science Foundation (Grant No. 19-72-00031).

[1] K. D. Behler, A. Stravato, V. Mochalin, G. Korneva, G. Yushin, and Y. Gogotsi, ACS Nano **3**, 363 (2009).

[2] S. V. Kidalov and F. M. Shakhov, Materials **2**, 2467 (2009).

[3] Y. Xia, H. Yang, and C. T. Campbell, Acc. Chem. Res. **46**, 1671 (2013).

[4] M. Veldhorst, J. Hwang, C. Yang, A. Leenstra, B. de Ronde, J. Dehollain, J. Muhonen, F. Hudson, K. Itoh, A. Morello *et al.*, Nat. Nanotechnol. **9**, 981 (2014).

[5] Y.-C. Chen, P. S. Salter, S. Knauer, L. Weng, A. C. Frangeskou, C. J. Stephen, S. N. Ishmael, P. R. Dolan, S. Johnson, B. L. Green, G. W. Morley, M. E. Newton, J. G. Rarity, M. J. Booth, and J. M. Smith, Nat. Photon. **11**, 77 (2017).

[6] P. Andrich, F. Charles, X. Liu, H. L. Bretscher, J. R. Berman, F. J. Heremans, P. F. Nealey, and D. D. Awschalom, npj Quantum Inf. **3**, 28 (2017).

[7] D. Riedel, I. Söllner, B. J. Shields, S. Starosielec, P. Appel, E. Neu, P. Maletinsky, and R. J. Warburton, Phys. Rev. X **7**, 031040 (2017).

[8] Y. Lin, X. Sun, D. S. Su, G. Centi, and S. Perathoner, Chem. Soc. Rev. **47**, 8438 (2018).

[9] V. Pichot, M. Guerchoux, O. Muller, M. Guillevic, P. Fioux, L. Merlat, and D. Spitzer, Diam. Relat. Mater. **95**, 55 (2019).

[10] O. Faklaris, V. Joshi, T. Irinopoulou, P. Tauc, M. Sennour, H. Girard, C. Gesset, J.-C. Arnault, A. Thorel, J.-P. Boudou *et al.*, ACS Nano **3**, 3955 (2009).

[11] M. A. Walling, J. A. Novak, and J. R. Shepard, Int. J. Mol. Sci. **10**, 441 (2009).

[12] J.-H. Park, L. Gu, G. Von Maltzahn, E. Ruoslahti, S. N. Bhatia, and M. J. Sailor, Nat. Mater. **8**, 331 (2009).

[13] J.-C. Arnault, in *Novel Aspects of Diamond*, edited by N. Yang, Topics in Applied Physics (Springer International Publishing, Cham, Switzerland, 2015), Vol. 121, pp. 85–122.

[14] S. E. Kim, L. Zhang, K. Ma, M. Riegman, F. Chen, I. Ingold, M. Conrad, M. Z. Turker, M. Gao, X. Jiang *et al.*, Nat. Nanotechnol. **11**, 977 (2016).

[15] D. A. Kurdyukov, D. A. Eurov, S. V. Shmakov, D. A. Kirilenko, J. A. Kukushkina, A. N. Smirnov, M. A. Yagovkina, V. V. Klimenko, S. V. Koniakhin, and V. G. Golubev, Microp. Mesop. Mater. **281**, 1 (2019).

[16] S. Mourdikoudis, R. M. Pallares, and N. T. Thanh, Nanoscale **10**, 12871 (2018).

[17] M. Calvaresi, Nat. Nanotechnol. **15**, 512 (2020).

[18] M. Yoshikawa, Y. Mori, M. Maegawa, G. Katagiri, H. Ishida, and A. Ishitani, Appl. Phys. Lett. **62**, 3114 (1993).

[19] M. Yoshikawa, Y. Mori, H. Obata, M. Maegawa, G. Katagiri, H. Ishida, and A. Ishitani, Appl. Phys. Lett. **67**, 694 (1995).

[20] O. A. Shenderova, I. I. Vlasov, S. Turner, G. Van Tendeloo, S. B. Orlinskii, A. A. Shiryaev, A. A. Khomich, S. N. Sulyanov, F. Jelezko, and J. Wrachtrup, J. Phys. Chem. C **115**, 14014 (2011).

[21] M. V. Korobov, D. S. Volkov, N. V. Avramenko, L. A. Belyaeva, P. I. Semenyuk, and M. A. Proskurnin, Nanoscale **5**, 1529 (2013).

[22] S. Stehlik, M. Varga, M. Ledinsky, V. Jirasek, A. Artemenko, H. Kozak, L. Ondic, V. Skakalova, G. Argentero, T. Pennycook, J. C. Meyer, A. Fejfar, A. Kromka, and B. Rezek, J. Phys. Chem. C **119**, 27708 (2015).

[23] S. Stehlik, M. Varga, M. Ledinsky, D. Miliaieva, H. Kozak, V. Skakalova, C. Mangler, T. J. Pennycook, J. C. Meyer, A. Kromka *et al.*, Sci. Rep. **6**, 38419 (2016).

[24] S. Koniakhin, N. Besedina, D. Kirilenko, A. Shvidchenko, and E. Eidelman, Superlatt. Microstruct. **113**, 204 (2018).

[25] A. Dideikin, A. Aleksenskii, M. Baidakova, P. Brunkov, M. Brzhezinskaya, V. Y. Davydov, V. Levitskii, S. Kidalov, Y. A. Kukushkina, D. Kirilenko *et al.*, Carbon **122**, 737 (2017).

[26] S. L. Chang, C. Dwyer, E. Osawa, and A. S. Barnard, Nanoscale Horizons **3**, 213 (2018).

[27] R. Bahariqushchi, S. Gündoğdu, and A. Aydinli, Superlatt. Microstruct. **111**, 90 (2017).

[28] Y. Kwon, J. Oh, E. Lee, S. H. Lee, A. Agnes, G. Bang, J. Kim, D. Kim, and S. Kim, Nat. Commun. **11**, 1 (2020).

[29] S. V. Koniakhin, M. K. Rabchinskii, N. A. Besedina, L. V. Sharonova, A. V. Shvidchenko, and E. D. Eidelman, Phys. Rev. Res. **2**, 013316 (2020).

[30] T. Kovářík, P. Bělský, D. Rieger, J. Ilavsky, V. Jandová, M. Maas, P. Šutta, M. Pola, and R. Medlín, J. Nanopart. Res. **22**, 34 (2020).

[31] H. Richter, Z. Wang, and L. Ley, Solid State Commun. **39**, 625 (1981).

[32] I. Campbell and P. M. Fauchet, Solid State Commun. **58**, 739 (1986).

[33] S. V. Koniakhin, O. I. Utesov, I. N. Terterov, A. V. Siklitskaya, A. G. Yashenkin, and D. Solnyshkov, J. Phys. Chem. C **122**, 19219 (2018).

[34] O. I. Utesov, A. G. Yashenkin, and S. V. Koniakhin, J. Phys. Chem. C **122**, 22738 (2018).

[35] J. Zi, K. Zhang, and X. Xie, Phys. Rev. B **55**, 9263 (1997).

[36] A. Meilakhs and S. Koniakhin, Superlatt. Microstruct. **110**, 319 (2017).

[37] Y. Gao and P. Yin, Diam. Relat. Mater. **99**, 107524 (2019).

[38] V. N. Mochalin, O. Shenderova, D. Ho, and Y. Gogotsi, Nat. Nanotechnol. **7**, 11 (2012).

[39] V. I. Korepanov, H. Hamaguchi, E. Osawa, V. Ermolenkov, I. K. Lednev, B. J. Etzold, O. Levinson, B. Zousman, C. P. Epperla, and H.-C. Chang, Carbon **121**, 322 (2017).

[40] V. I. Korepanov and H. Hamaguchi, J. Raman Spectrosc. **48**, 842 (2017).

[41] V. I. Korepanov, J. Raman Spectrosc. **51**, 881 (2020).

[42] W. Ke, X. Feng, and Y. Huang, J. Appl. Phys. **109**, 083526 (2011).

[43] G. Faraci, S. Gibilisco, P. Russo, A. R. Pennisi, and S. La Rosa, Phys. Rev. B **73**, 033307 (2006).

[44] O. I. Utesov, A. G. Yashenkin, and S. V. Koniakhin, Phys. Rev. B **102**, 205421 (2020).

[45] A. G. Yashenkin, O. I. Utesov, and S. V. Koniakhin, arXiv:2004.12631.

[46] M. Born and K. Huang, *Dynamical Theory of Crystal Lattices* (Clarendon Press, Oxford, 1954).

[47] A. Maradudin, E. Montroll, G. Weiss, and I. Ipatova, in *Theory of Lattice Dynamics in the Harmonic Approximation*, Solid State Physics, Supplements (Academic Press, New York, 1971), Vol. 3, p. 582.

[48] P. Keating, Phys. Rev. **145**, 637 (1966).

[49] R. M. Martin, Phys. Rev. B **1**, 4005 (1970).

[50] E. Kane, Phys. Rev. B **31**, 7865 (1985).

[51] S. Steiger, M. Salmani-Jelodar, D. Areshkin, A. Paul, T. Kubis, M. Povolotskyi, H.-H. Park, and G. Klimeck, Phys. Rev. B **84**, 155204 (2011).

[52] E. Anastassakis, A. Cantarero, and M. Cardona, Phys. Rev. B **41**, 7529 (1990).

[53] Mathematica, Version 11.0, Wolfram Research, Inc., Champaign, Illinios, 2010.
[54] O. I. Utesov, A. V. Sizanov, and A. V. Syromyatnikov, Phys. Rev. B **90**, 155121 (2014).
[55] M. W. Doherty, N. B. Manson, P. Delaney, F. Jelezko, J. Wrachtrup, and L. C. Hollenberg, Phys. Rep. **528**, 1 (2013).
[56] H. Stöckmann, Scholarpedia **5**, 10243 (2010).
[57] A. C. Ferrari and J. Robertson, Philos. Trans. R. Soc. London A **362**, 2477 (2004).
[58] V. Popov, A. Egorov, S. Savilov, V. Lunin, A. Kirichenko, V. Denisov, V. Blank, O. Vyaselev, and T. Sagalova, J. Surf. Invest.: X-Ray, Synchrotron Neutron Tech. **7**, 1034 (2013).
[59] P. Kehayias, M. W. Doherty, D. English, R. Fischer, A. Jarmola, K. Jensen, N. Leefer, P. Hemmer, N. B. Manson, and D. Budker, Phys. Rev. B **88**, 165202 (2013).
[60] A. Gali, T. Simon, and J. Lowther, New J. Phys. **13**, 025016 (2011).
[61] E. Ekimov, S. Lyapin, A. Razgulov, and M. Kondrin, J. Exp. Theor. Phys. **129**, 855 (2019).
[62] Á. Gali, Nanophotonics **8**, 1907 (2019).
[63] D. S. Bethune, G. Meijer, W. C. Tang, H. J. Rosen, W. G. Golden, H. Seki, C. A. Brown, and M. S. de Vries, Chem. Phys. Lett. **179**, 181 (1991).
[64] J. Filik, J. N. Harvey, N. L. Allan, P. W. May, J. E. P. Dahl, S. Liu, and R. M. K. Carlson, Phys. Rev. B **74**, 035423 (2006).
[65] A. Aleksenskii, M. Baidakova, A. Y. Vul', V. Y. Davydov, and Y. A. Pevtsova, Phys. Solid State **39**, 1007 (1997).
[66] M. Mermoux, S. Chang, H. A. Girard, and J.-C. Arnault, Diam. Relat. Mater. **87**, 248 (2018).
[67] S. Osswald, V. N. Mochalin, M. Havel, G. Yushin, and Y. Gogotsi, Phys. Rev. B **80**, 075419 (2009).
[68] J. Holzgrafe, Q. Gu, J. Beitner, D. M. Kara, H. S. Knowles, and M. Atatüre, Phys. Rev. Appl. **13**, 044004 (2020).
[69] C. Meier, S. Lüttjohann, V. G. Kravets, H. Nienhaus, A. Lorke, and H. Wiggers, Physica E **32**, 155 (2006).
[70] J. Gleize, F. Demangeot, F. Frandon, M. Renucci, M. Kuball, F. Widmann, and B. Daudin, Phys. Status Solidi (b) **216**, 457 (1999).
[71] E. Giulotto, M. Geddo, M. Grandi, G. Guizzetti, G. Trevisi, L. Seravalli, P. Frigeri, and S. Franchi, Appl. Phys. Lett. **98**, 111903 (2011).
[72] K. C. Hass, M. A. Tamor, T. R. Anthony, and W. F. Banholzer, Phys. Rev. B **45**, 7171 (1992).
[73] T. Nakayama, K. Yakubo, and R. L. Orbach, Rev. Mod. Phys. **66**, 381 (1994).
[74] M. Chaigneau, G. Picardi, H. A. Girard, J.-C. Arnault, and R. Ossikovski, J. Nanopart. Res. **14**, 955 (2012).